Monthly Notices
of the
ROYAL ASTRONOMICAL SOCIETY

Mon. Not. R. Astron. Soc. **409,** 639–661 (2010) doi:10.1111/j.1365-2966.2010.17327.x

On the dynamics of planetesimals embedded in turbulent protoplanetary discs

Richard P. Nelson★ and Oliver Gressel★

Astronomy Unit, Queen Mary, University of London, Mile End Road, London E1 4NS

Accepted 2010 July 7. Received 2010 July 5; in original form 2010 April 29

ABSTRACT

Angular momentum transport and accretion in protoplanetary discs are generally believed to be driven by magnetohydrodynamics (MHD) turbulence *via* the magnetorotational instability (MRI). The dynamics of solid bodies embedded in such discs (dust grains, boulders, planetesimals and planets) may be strongly affected by the turbulence, such that the formation pathways for planetary systems are determined in part by the strength and spatial distribution of the turbulent flow.

We examine the dynamics of planetesimals, with radii between 1 m and 10 km, embedded in turbulent protoplanetary discs, using 3D MHD simulations. The planetesimals experience gas drag and stochastic gravitational forces due to the turbulent disc. We use, and compare the results from, local shearing box simulations and global models in this study.

The main aims of this work are to examine: the growth, and possible saturation, of the velocity dispersion of embedded planetesimals as a function of their size and disc parameters; the rate of radial migration and diffusion of planetesimals; the conditions under which the results from shearing box and global simulations agree.

We find good agreement between local and global simulations when shearing boxes of dimension $4H \times 16H \times 2H$ are used (H being the local scaleheight). The magnitude of the density fluctuations obtained is sensitive to the box size, due to the excitation and propagation of spiral density waves. This affects the stochastic forcing experienced by planetesimals. The correlation time associated with the stochastic forcing is also found to be a function of the box size and aspect ratio.

The equilibrium radial velocity dispersion, $\sigma(v_r)$, obtained depends on the radii, R_p, of the planetesimals. Bodies with $R_p = 50$ m achieve the smallest value with $\sigma(v_r) \simeq 20\,\mathrm{m\,s^{-1}}$. Smaller bodies are tightly coupled to the gas, and boulders with $R_p = 1$ m attain a value of $\sigma(v_r)$ similar to the turbulent velocity of the gas ($\sim 100\,\mathrm{m\,s^{-1}}$). Equilibrium values of $\sigma(v_r)$ for bodies larger than 100 m are not achieved in our simulations, but in all models we find rapid growth of the velocity dispersion for planetesimals of size 1 and 10 km, such that $\sigma(v_r) \geq 160\,\mathrm{m\,s^{-1}}$ after a run time of 1200 orbits at a distance of 5 au from the central star. These values are too large to allow for the runaway growth of planetesimals, and mutual collisions would lead to catastrophic disruption. Radial migration due to gas drag is observed for bodies with $R_p \simeq 1$ m, and is only modestly affected by the turbulence. Larger bodies undergo a random walk in their semimajor axes, leading to radial diffusion through the disc. For our fiducial disc model, we estimate that radial diffusion across a distance of $\simeq$2.5 au would occur for typical planetesimals in a swarm located at 5 au over a disc lifetime of 5 Myr. Radial diffusion of this magnitude appears to be inconsistent with Solar system constraints.

Our models show that fully developed magnetohydrodynamics (MHD) turbulence in protoplanetary discs would have a destructive effect on embedded planetesimals. Relatively low levels of turbulence are required for traditional models of planetesimal accretion to operate, this being consistent with the existence of a dead zone in protoplanetary discs.

Key words: accretion, accretion discs – MHD – methods: numerical – planets and satellites: formation – protoplanetary discs.

★E-mail: r.p.nelson@qmul.ac.uk (RPN); o.gressel@qmul.ac.uk (OG)

1 INTRODUCTION

The dynamical and collisional evolution of planetesimals is a fundamental issue which needs to be understood if progress is to be made in developing a theory of planetary system formation. According to the core accretion theory, a process which begins with the collision and sticking of small dust grains within a protoplanetary disc leads eventually to the formation of kilometre-sized planetesimals (Wetherill & Stewart 1993). Although alternative scenarios have been put forward for planetesimal formation (Goldreich & Ward 1973; Johansen et al. 2007), which avoid the requirement for such large bodies to grow *via* simple two-body agglomeration processes, the further growth of planetesimals into planetary embryos and cores generally requires planetesimals themselves to accrete *via* mutual collisions through a process of runaway growth, followed by oligarchic growth (Ida & Makino 1993; Kokubo & Ida 1998).

Rapid runaway growth requires that the velocity dispersion of the planetesimal swarm remains significantly smaller than the escape velocity from the surfaces of the largest accreting planetesimals, ensuring that gravitational focusing is important. For bodies of radius 10 km, and with internal densities $\varrho_{\rm p} \simeq 2\,{\rm g\,cm^{-3}}$, the escape velocity is $10\,{\rm m\,s^{-1}}$, and scales linearly with radius. Clearly this is a stringent requirement, which is easily met within a self-stirring planetesimal swarm whose size distribution is reasonably shallow, but which may be difficult to satisfy in the presence of an external source of stirring. One such source may be turbulence within the protoplanetary disc. Planetary growth times which rely on mutual collisions between planetesimals occurring at rates which are determined by the geometric cross-section are prohibitively long, leading to estimated planetary growth times which are much in excess of typical protostellar disc lifetimes (Haisch, Lada & Lada 2001).

A further constraint during the runaway growth phase is that collisional velocities should be small enough to avoid catastrophic disruption of planetesimals. For bodies in the 1–10 km size range, for which self-gravity starts to become more important than material strength in holding planetesimals together, collisions between similar-sized bodies with impact speeds which are modestly in excess of the escape velocity will lead to breakup of the planetesimals rather than accretion and growth. Indeed Benz & Asphaug (1999) suggest that mutual collisions between 1 km sized bodies will result in catastrophic disruption if the impact speeds exceed $\sim 20\,{\rm m\,s^{-1}}$, depending on the material composition of the impactors. In a more recent study, Stewart & Leinhardt (2009) suggest reduced impact speeds of $\sim 10\,{\rm m\,s^{-1}}$ will be destructive. Once again, we see that an external source of planetesimal stirring may prevent the rapid growth of planetary mass bodies by the accretion of planetesimals.

The canonical mass accretion rate for T Tauri stars is $\sim 10^{-8}\,{\rm M_\odot\,yr^{-1}}$ (Sicilia-Aguilar et al. 2004). Such accretion rates require a source of anomalous disc viscosity and angular momentum transport to operate, generally thought to be turbulence. The most likely source of disc turbulence is the magnetorotational instability (MRI; Balbus & Hawley 1991) which has been shown to develop into full non-linear magnetohydrodynamics (MHD) turbulence in numerous studies, using both local shearing box simulations (Hawley, Gammie & Balbus 1995) and global simulations (Armitage 1998; Hawley 2001; Papaloizou & Nelson 2003). The nature and saturation state of MHD turbulence generated by the MRI is the subject of on-going study (Fromang & Papaloizou 2007; Fromang et al. 2007). In this work, we use the dependence of the turbulent stresses and density fluctuation amplitude on the strength of the net component of the magnetic field to examine the evolution of planetesimals in discs with different levels of turbulence. We use simple disc models, which neglect non-ideal MHD effects and vertical stratification. As such, this is the first in a series of papers in which we examine how turbulence affects the dynamics of planetesimals embedded in turbulent discs. Future papers will explore the effects of vertical stratification and dead zones.

There have been numerous studies of planets embedded in turbulent protoplanetary discs. Nelson & Papaloizou (2003) and Winters, Balbus & Hawley (2003) examined the formation of gaps by Jovian mass planets, and the migration torques exerted by the disc on the planet. Nelson & Papaloizou (2004) performed global simulations of low-mass planets embedded in turbulent discs. They showed that such bodies are subject to fluctuating torques which should induce stochastic migration, and suggested that this might provide a means of mitigating against the rapid type I migration expected to occur for low-mass planets (Ward 1997). Laughlin, Steinacker & Adams (2004) published a similar study using analytical fits to MHD simulations, and reached similar conclusions. Papaloizou, Nelson & Snellgrove (2004) presented results from both global and local shearing box simulations containing both high- and low-mass planets, and showed good agreement between the simulation set-ups for predicting the transition between linear and non-linear disc response to the presence of an embedded planet. In a follow-up paper, Nelson (2005) examined the orbital evolution of low-mass embedded planets, showing that over simulations run times of $\simeq$100 orbits, turbulence induces stochastic migration for planets in the range 1–10 $\rm M_\oplus$, and induces the growth of orbital eccentricity. In a more recent work, Oishi, Mac Low & Menou (2007) examined the stochastic forces experienced by planets in stratified disc models with and without dead zones using shearing box simulations, and Yang, Mac Low & Menou (2009) examined the orbital evolution of swarms of test particles embedded in non-stratified turbulent discs.

A significant volume of related work has examined the influence of disc turbulence on embedded planets and planetesimals using prescriptions or simple models for the effects of turbulence. Johnson, Goodman & Menou (2006) developed a Fokker–Planck description for the stochastic evolution of planets, and examined the survival probabilities of distributions of planets subject to type I migration and superposed stochastic migration. A similar study has been published recently by Adams & Bloch (2009). Ogihara, Ida & Morbidelli (2007) have used *N*-body simulations plus a prescription for stochastic forcing to examine the effects of turbulence on terrestrial planet formation. Ida, Guillot & Morbidelli (2008) used a similar prescription of turbulent forcing and examined the growth of eccentricity for planetesimals, exploring in particular the possibility of reaching catastrophic disruption velocities. Adams, Laughlin & Bloch (2008) and Rein & Papaloizou (2009) examined the stability of mean motion resonances for pairs of planets embedded in turbulent discs, and Baruteau & Lin (2010) have examined the saturation of corotation torques in turbulent discs by means of hydrodynamic simulations subject to turbulent stirring.

In this paper, we examine in detail the orbital evolution of planetesimals of different size (ranging between 1 m and 10 km) embedded in turbulent disc models by means of 3D MHD simulations. A key issue that we explore is the set of conditions and numerical parameters that provide good agreement between local shearing box simulations and global simulations. We find that it is possible to obtain good agreement between these two numerical set-ups, provided that the shearing box dimensions are chosen appropriately. Other important issues that we examine include the growth of the velocity dispersion of embedded swarm of planetesimals, and the saturation value of this velocity dispersion as a function of planetesimal size due to a balance being achieved between gas drag and turbulent

forcing. We explore the implications of our results for the efficiency of runaway growth of planetary embryos, and the possibility that planetesimals may enter a phase of catastrophic disruption through mutual collisions. We also examine the rate at which planetesimals migrate due to both gas drag induced radial drift (Weidenschilling 1977), and diffusion caused by the fluctuating gravitational field of the turbulent disc. We examine under which conditions each of these processes is dominant, and we explore the implications of our results for the radial drift of planetesimals in the solar nebula and limits that might be placed on the magnitude of turbulent fluctuations which were present during the early phases of Solar system formation.

This paper is organized as follows. In Section 2, we describe the numerical set-up and the parameters of the disc models. In Section 3 we present our results. In Section 4 we discuss our work in the context of previous work and draw our conclusions.

2 MODEL DESCRIPTION

We perform self-consistent simulations of hydromagnetic turbulence using two different set-ups: shearing box simulations which represent a local patch of a protoplanetary disc; global disc models which simulate a larger section of a protoplanetary disc and include the full set of curvature terms in the equations of motion. A major goal of this work is to compare the results of these two different approaches.

A key question that needs to be addressed is for what dimensions of the shearing box, in units of the local scaleheight H, do density fluctuations created by the turbulence reach a converged amplitude and spectrum, and do these match the results of global models. To make the comparison as straightforward as possible, we neglect vertical stratification and assume an isothermal equation of state.

In both configurations, the hydromagnetic turbulence is driven via the non-linear development of the MRI. At present, the issue of the saturated amplitude of MRI turbulence remains unresolved and is a topic of active research (Fromang & Papaloizou 2007; Fromang et al. 2007). In the absence of a better alternative, we therefore adopt a practical perspective and impose a net vertical or azimuthal flux, for which numerical convergence can be obtained (Davis, Stone & Pessah 2010). Neglecting the dependence on the magnetic Prandtl number (Lesur & Longaretti 2007), we furthermore restrict ourselves to the case of ideal MHD. This approach is justified by the observed correlation between the strength of the turbulence and the amplitude of the resulting density fluctuations (Yang et al. 2009). This means that we regard the strength of the imposed field as a control parameter which can be tuned to vary the turbulence amplitude in the local and global context. The global cylindrical disc models are computed with a modified version of the original finite difference code NIRVANA (Ziegler & Yorke 1997). For the local shearing box models, we make use of the newly developed second-order Godunov code NIRVANA-III (Ziegler 2004, 2008).

2.1 Numerical methods – local model

For our standard model, we adopt a box size[1] of $4 \times 16 \times 2$ pressure scaleheights H at a resolution of 32 grid points per H. Boundary conditions are periodic in the azimuthal (y) and vertical (z), and sheared-periodic in the radial (x) direction. The initial net vertical magnetic field corresponds to a plasma parameter $\beta \simeq 6000$ (i.e. the ratio of thermal to magnetic pressure), resulting in a typical saturation level $\alpha \simeq 0.05$ of the turbulence, where α is the effective viscosity parameter (Shakura & Syunyaev 1973).

Because the gas drag forces acting on massive particles depend on the actual physical value of the gas density, we have to prescribe a set of conversion factors to link our model to a representative protoplanetary disc. We chose a fiducial radius $R_0 = 5$ au, and a geometric disc thickness of $H/R = 0.05$ at $R = 1$ au. Note that this aspect ratio is scaled with $R^{1/4}$ to be consistent with the Hayashi minimum mass solar nebula (MMSN; Hayashi 1981), yielding a value of $\simeq$0.075 at 5 au. Furthermore, we chose a slightly higher average mass density than in this model to yield a column density $\Sigma = 160\,\mathrm{g\,cm^{-2}}$ and sound speed $c_\mathrm{s} = 1\,\mathrm{km\,s^{-1}}$ comparable to the global simulations.

For the local model, we evolve the following set of non-linear partial differential equations:

$$\begin{aligned} \partial_t \varrho + \nabla \cdot (\varrho \mathbf{v}) &= 0, \\ \partial_t (\varrho \mathbf{v}) + \nabla \cdot \left[\varrho \mathbf{v}\mathbf{v} + \left(p + \frac{\mathbf{B}^2}{2\mu} \right) I - \frac{\mathbf{B}\mathbf{B}}{\mu} \right] &= -2\varrho\Omega\,\hat{\mathbf{z}} \times (\mathbf{v} + q\Omega x\,\hat{\mathbf{y}}) \\ \partial_t \mathbf{B} - \nabla \times (\mathbf{v} \times \mathbf{B}) &= 0, \end{aligned} \tag{1}$$

comprising the standard formulation of ideal MHD in the shearing box approximation, and where we have assumed an isothermal equation of state $p = \varrho c_\mathrm{s}^2$ and neglected the effects of stratification. The two momentum source terms are the Coriolis force $-2\Omega\hat{\mathbf{z}} \times \mathbf{v}$ in the locally corotating frame, and the tidal term $2q\Omega^2 x\,\hat{\mathbf{x}}$, with shear-parameter $q = 3/2$, describing the linearized effect of the Keplerian rotation.[2] Care has been taken in implementing the source terms to minimize the error in the epicyclic mode energy (Gressel & Ziegler 2007), albeit not to the extent where it is conserved to machine accuracy (Stone & Gardiner 2010).

2.1.1 *Numerical scheme and orbital advection*

As has been recently demonstrated by Balsara & Meyer (2010), the adequate modelling of the MRI with finite volume codes depends on the reconstruction strategy used and, in particular, on the ability of the Riemann solver to capture the Alfvén mode. To improve the treatment of discontinuities in the Godunov scheme, we therefore extended NIRVANA-III with the Harten–Lax–van Leer Discontinuities (HLLD) approximate Riemann solver proposed by Miyoshi & Kusano (2005).

In accordance with its finite volume approach, the NIRVANA-III code evaluates the components of the electromotive force (EMF) at cell interfaces. Since the discretization of the constrained transport algorithm intrinsically requires edge-aligned EMFs, some sort of interpolation is required. In its original form, NIRVANA-III implements the arithmetic average proposed by Balsara & Spicer (1999). As discussed in section 3.2 of Gardiner & Stone (2005), this approach however lacks the required directional biasing to guarantee the stability of the numerical scheme. It has further been demonstrated by Flock et al. (2010) that this can lead to artificial growth of instabilities in the context of net-flux MRI, and we have reproduced this result. To resolve this issue, we have successfully implemented and tested the upwind reconstruction procedure of Gardiner & Stone (2005).

Following the long-term evolution of a shearing flow in boxes of substantial radial extent puts high demands on computational

[1] See Section 3.3 for a discussion on the effect of the box size.

[2] The variable $x = R - R_0$ is the radial displacement from the box centre.

resources. For a Keplerian rotation profile, the background flow becomes super-sonic for $L_x > 4/3H$. This implies that for increasingly larger boxes the numerical time-step, defined by the Courant condition, becomes dominated by the unperturbed shear profile. To circumvent this undesirable constraint, it becomes mandatory to split-off the transport term due to the background profile.

The shear transport is usually implemented in terms of an interpolation step. This was first introduced in cylindrical geometry and termed FARGO by Masset (2000). Later, the method was adopted to the local shearing box model by Gammie (2001).

A rather intricate extension for the induction equation that requires mapping of the magnetic field components has been proposed by Johnson, Guan & Gammie (2008). We here follow the (much simpler) constrained transport approach proposed by Stone & Gardiner (2010), which by construction preserves the solenoidal constraint.

For our implementation of the orbital advection scheme, we operator-split the advection step from the Runge–Kutta time integration of the remaining terms. For the interpolation of the fluid variables, we make use of the high-order Fourier scheme [shear advection by Fourier interpolation (SAFI)] described in appendix B of Johansen, Youdin & Klahr (2009).

We similarly apply SAFI to obtain the non-integer part of the line-integrals which contribute the circulation of the electric fields entering the induction equation (cf. equations 61 and 62 in Stone & Gardiner 2010). The treatment of the magnetic source term in the total energy equation can be successfully avoided if the magnetic energy is removed from the total energy during the interpolation. The implementation has been tested with the advection of a field loop (Gardiner & Stone 2008), and the exact wave solution given in Balbus & Hawley (2006).

Using SAFI rather than slope-limited linear interpolation, efficiently reduces the dissipation due to the transport step, and moreover its dependence on position (see Johansen et al. 2009). In fact, the scheme adds so little dissipation that the total variation diminishing (TVD) requirement might be violated. To formally make the interpolation TVD, we therefore discard the Fourier mode corresponding to the Nyquist frequency.

2.1.2 Particle dynamics

In this paper, we restrict ourselves to the study of how disc turbulence affects embedded particle populations. Neglecting their back reaction on the flow, particles are hence treated as passive test bodies which do not interact mutually either through physical collisions or through gravity. Under these assumptions, we ignore the possibility of increasing the velocity dispersion of particles via mutual gravitational scattering. While this effect might become important for $\sim 10^2$ km-sized objects, it simply adds to the external stirring. Physical collisions between planetesimals, however, can provide a source of damping. This effect was considered by Ida et al. (2008), and was found to be important in determining the equilibrium velocity dispersion only for bodies with size <1 km, and so we do not consider this effect in this paper. Moreover, because the particles cannot exert drag forces on the gas, our approach excludes collective effects such as the streaming instability (Youdin & Goodman 2005), which is a focus of current numerical studies (Youdin & Johansen 2007; Balsara et al. 2009; Bai & Stone 2010; Miniati 2010).

We include different species of particles to quantify various aspects of the flow. First, massless tracer particles (which instantaneously follow the gas velocity) measure the Lagrangian diffusion of the flow. This is relevant for small dust grains which are tightly coupled to the gas. Secondly, we include particles representing planetesimals. These particles interact with the flow *via* the gravitational potential produced by the gas density, and through the aerodynamic drag force. The relative importance of these effects is expected to change for planetesimals in the size range 1 m to 10 km, which are the subject of this study. Finally, for the purpose of comparison, and as a proxy for larger objects (e.g. small protoplanets), we include swarms of particles which experience gas gravity but are not subject to an aerodynamic drag force. With the exception of the tracers, all particles are subject to the local dynamics, i.e. they experience the Coriolis force in the rotating frame and the tidal force stemming from the local expansion of the Keplerian rotation profile. As a consequence, planetesimals generally perform epicyclic oscillations of fluctuating amplitude, around a stochastically migrating guiding centre.

2.2 Numerical method – global model

In the global simulations, we solve essentially the same set of equations for ideal MHD as described in Section 2.1 for the shearing box runs, except that we adopt cylindrical coordinates (r, ϕ, z) (see Nelson 2005 for a full description). The simulations are performed in a rotating frame with angular frequency equal to the Keplerian frequency at the midpoint of the radial computational domain. We use a locally isothermal equation of state

$$P(r) = c_s(r)^2 \, \varrho, \tag{2}$$

where $c_s(r)$ denotes the sound speed which is specified as a fixed function of r. The models investigated may be described as cylindrical discs (e.g. Hawley 2001), in which the gravitational potential is taken to depend on r alone. Thus, the cylindrical disc models do not include a full treatment of the disc vertical structure. Models of this type are employed due to the high computational overhead that would be required to fully resolve the disc vertical structure of a stratified model.

The global simulations presented in this paper were performed using an older version of NIRVANA, which uses an algorithm very similar to the ZEUS code to solve the equations of ideal MHD (Stone & Norman 1992; Ziegler & Yorke 1997). This scheme uses operator splitting, dividing the governing equations into source terms and transport terms. Advection is performed using the second-order monotonic transport scheme (van Leer 1977), and the magnetic field is evolved using the Method of Characteristics Constrained Transport (Hawley & Stone 1995).

2.2.1 Gas disc model

The main aim of this paper is to examine the orbital evolution of planetesimals and smaller bodies (boulders) in turbulent discs, where the disc turbulence has achieved a well-defined steady state. Another aim is to compare local shearing box runs with global simulations. To achieve these aims, most of the global disc models were chosen to have a relatively narrow radial extent, and azimuthal domains running between $0 \leq \phi \leq \pi/2$. The turbulent stresses generated within a global disc lead to significant changes in the radial density distribution, such that the properties of the disc deviate substantially from a statistical steady state over runs times of 100 s of orbits (Papaloizou & Nelson 2003). In order to overcome this, we have introduced an additional equation to be solved alongside equations (1) in the global simulations, whose purpose is to maintain

a roughly constant surface density profile during the runs:

$$\frac{\mathrm{d}\varrho(t)}{\mathrm{d}t} = -\frac{\varrho(t) - \varrho_0}{\tau_\mathrm{m}}. \quad (3)$$

Here $\varrho(t)$ is the density at each spatial location in the disc at time t, ϱ_0 is the initial density defined at each location in the disc and τ_m is the characteristic time on which the local perturbed density evolves back towards its original value. Clearly, if τ_m is shorter than any relevant local dynamical time in the disc, then perturbations will be damped very quickly and the disc will not be able to achieve a turbulent state. Similarly, if τ_m is much longer than the longest (viscous) evolution time in the disc, the global density profile will be able to evolve to be very different from the initial one. By choosing τ_m to be intermediate between these two extremes, we find that our global disc models are able to develop a well-defined turbulent state, in which the turbulence is able to maintain an approximate statistical steady state over long time-scales ($>10^3$ orbits). We have found that $\tau_\mathrm{m} = 50$ orbits measured at the radial midpoint of the disc model provides a model with the desired properties.

A possible alternative to solving equation (3) would be to feed in mass at the outer radial boundary at the requisite rate. Such an approach works well as a means of generating a steady disc when the disc is laminar and employs the α-model for viscosity (Masset 2002). In a turbulent disc, where there is substantial temporal and spatial variation in the viscous stress, however, such an approach may not be effective at maintaining a well-defined surface density profile.

2.2.2 *Initial and boundary conditions*

Each global model has a value for the inner and outer radii of the computational domain, r_in and r_out, a value for the height of the upper and lower 'surfaces' of the disc, Z_min and Z_max, and minimum and maximum values of the azimuthal angle, ϕ_min and ϕ_max. These values are tabulated in Table 1, along with some of the physical parameters described below. The resolution used in each simulation covering $\pi/2$ in azimuth was $(N_\mathrm{r}, N_\phi, N_z) = (160, 320, 40)$. For the model covering 2π in azimuth $N_\phi = 1280$. This corresponds to 10 cells per mean scaleheight in the radial and azimuthal directions, and 20 cells per scaleheight in the vertical domain. When considering the behaviour of the correlation time for the fluctuating torques in Section 3.3.1, we also ran models with double and quadruple the resolution in the radial and azimuthal directions.

The unit of length in our simulations is taken to be 2 au, such that a radial distance of $r = 2.5$ in computational units corresponds to 5 au. The unit of mass is assumed to be the solar mass. When we discuss the temporal evolution of our models later in the paper, we adopt a time unit which is equal to the orbital period at $r = 2.5$ (equivalent to 5 au); this being the midpoint of our radial domain.

The disc models we adopt are similar locally to the MMSN model (Hayashi 1981) at a distance of 5 au from the star. All models have a constant aspect ratio H/r, and all but one model has $H/r = 0.05$. Model G5 has $H/r = 0.075$ for the purpose of comparing directly with the local shearing box models (where this value of H/r was used). Initially, the density is constant, such that the surface density $\Sigma = 150\,\mathrm{g\,cm^{-3}}$.

The initial magnetic field in the global runs is purely toroidal, with the local field strength being determined from the local plasma β parameter ($\beta = P_\mathrm{gas}/P_\mathrm{mag}$). The value of β used in each run is tabulated in Table 1. The field is introduced at all locations in the disc, except near the radial boundaries where the field is set to zero for $r - r_\mathrm{in} < 0.1$ and $r_\mathrm{out} - r < 0.1$. The initial disc velocity is determined according to

$$v_\phi = r\sqrt{\frac{GM_*}{r^3}\left[1 - \left(\frac{H}{r}\right)^2\right]}, \quad (4)$$

where $M_\star$ is the mass of the central star, with the other velocity components being set to zero. Prior to a run being initiated, however, all velocity components are seeded with random noise with an amplitude equal to 5 per cent of the local sound speed.

Each disc model described in Table 1 was evolved until the turbulence reached a quasi-steady state before the planetesimals were inserted. Most runs included planetesimals of size 10 m, 100 m, 1 km and 10 km, with each size being represented by 25 particles. The planetesimals were distributed randomly in a narrow annulus centred on the computational radius $r = 2.5$ (equivalent to 5 au in physical units) of width $\Delta r = 0.2$, with their initial velocities calculated such that they are on circular orbits under the influence of the instantaneous gravitational potential of the central star and turbulent disc.

We adopt periodic boundary conditions at the vertical and azimuthal boundaries, and reflecting boundary conditions at the radial boundaries. Furthermore, we use wave damping boundary conditions in the vicinity of the radial boundaries using the scheme described in de Val-Borro et al. (2006). This scheme relaxes the velocity and density near the boundaries towards their initial values on a time-scale equal to 10 per cent of the local orbital period.

2.3 Gravitational forces

Both the local and the global models calculate the gravitational potential of the gas at the position of the particles via direct summation. This is computationally favourable as long as one is only interested in a relatively small number of particles. Since we do not consider collective effects, an ensemble of a few tens of members is usually sufficient to reasonably determine the time-averaged distribution of their positions and velocities.

For the integration of the gravitational force, the mass contained within a grid cell is treated as a point source located at the cell centre. To avoid artefacts due to close encounters, we apply a common smoothing length formalism with a parameter $b = (\delta_x^2 + \delta_y^2)^{1/2}$ equal to the diagonal across the cell.

Table 1. Global simulation parameters and results.

Simulation	$r_\mathrm{in}/r_\mathrm{out}$	ϕ_max	$Z_\mathrm{min}/Z_\mathrm{max}$	H/r	β	$\langle\alpha\rangle$	$\langle\delta\varrho/\varrho\rangle$	$\langle\delta\Sigma/\Sigma\rangle$	$C_\sigma(v_\mathrm{r})/(c_\mathrm{s}\times10^{-3})$	$C_\sigma(\Delta a)/(10^{-4})$
G0/G1	1.5/3.5	$\pi/2$	±0.125	0.05	50	0.035	0.143	0.109	8.87 ± 0.50	7.92 ± 0.69
G2	1.5/3.5	2π	±0.125	0.05	50	0.040	0.159	0.124	8.20 ± 0.32	12.20 ± 0.56
G3	1.5/3.5	$\pi/2$	±0.125	0.05	200	0.017	0.101	0.088	8.18 ± 0.41	7.17 ± 0.39
G4	1.5/3.5	$\pi/2$	±0.125	0.05	12.5	0.105	0.266	0.150	11.30 ± 0.70	10.00 ± 0.10
G5	1.0/4.0	$\pi/2$	±0.187	0.075	50	0.034	0.126	0.094	4.69 ± 0.21	7.65 ± 0.67

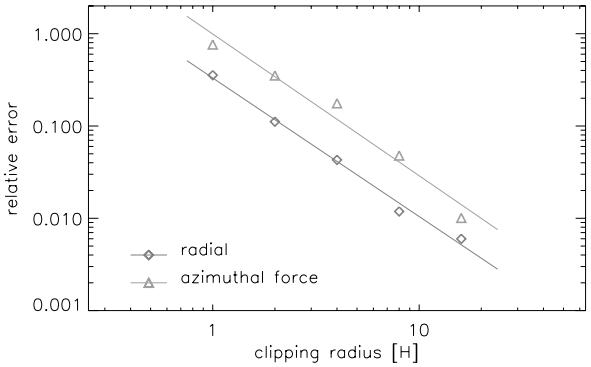

Figure 1. Convergence study regarding the computation of the gravitational force via direct summation; the convergence order is approximately 3/2.

As can be seen in fig. 2 of Heinemann & Papaloizou (2009b), the turbulence driven by long-wavelength MRI modes leads to the formation of strong density waves, which develop very little structure along the vertical direction. Accordingly, we neglect the vertical component of the forces and adopt a cylindrical description where the gravity now only depends on the vertically integrated column density. This approach greatly reduces the computational demand and is consistent with neglecting the vertical density stratification. As we will see in Section 3.3, this 2D treatment enhances the gravity forces by a factor of roughly 2.

When considering local shearing box simulations in particular, a question that needs to be answered is how large a shearing box is required before the gravitational forces from a turbulent disc are converged. In Fig. 1, we plot the relative error of the gravity force when integrating over spheres with increasing radius. We see that, for values accurate at the per cent level, one requires a sphere of influence with a radius of about 10 pressure scaleheights. As expected, forces in the azimuthal direction are affected more strongly by long-range contributions. Because the net effect is determined by density fluctuations, the convergence is weaker than the r^{-2} dependence for the Newtonian gravity. We consequently find a smaller convergence order of about 3/2. In our local simulations, we adopt a sphere (cylinder) with $r_{\rm cl} = 16H$, within which we compute the gravitational acceleration on a planetesimal, and suitably extend the domain by mirroring ghost domains according to the sheared periodicity.

In the global simulations the gravitational field is computed by summing over all grid cells. Most simulations were run using an azimuthal domain of $\pi/2$, although the planetesimal orbits cover the full 2π domain. When calculating the gravitational field experienced by the planetesimals, additional copies of the disc, each shifted by $n\pi/2$, where $n \in \{1, 2, 3\}$, are used to mimic a disc which covers the full 2π in azimuth. One run with a full 2π azimuthal domain was run to check that the above procedure gives accurate results.

2.4 Gas drag

For the gas drag, we use the usual formulae for the Stokes and Epstein regimes (Weidenschilling 1977; Rafikov 2004). In the Epstein regime, the drag force is given by

$$\boldsymbol{F}_{\rm drag} = (\boldsymbol{v}_{\rm g} - \boldsymbol{v}_{\rm p})\, \tau_{\rm s}^{-1}\,, \tag{5}$$

with the stopping time

$$\tau_{\rm s} = \frac{\varrho_{\rm p} R_{\rm p}}{\varrho c_{\rm s}}\,, \tag{6}$$

where $R_{\rm p}$ is the physical radius of the planetesimal, ϱ is the gas density at the position of the planetesimal, $\varrho_{\rm p}$ is the internal density of the planetesimal, $\boldsymbol{v}_{\rm p}$ is the planetesimal velocity and $\boldsymbol{v}_{\rm g}$ is the gas velocity. In the Stokes regime it may be written

$$\boldsymbol{F}_{\rm drag} = \frac{1}{2} C_{\rm D} \pi R_{\rm p}^2 \varrho\, |\boldsymbol{v}_{\rm p} - \boldsymbol{v}_{\rm g}|\, (\boldsymbol{v}_{\rm p} - \boldsymbol{v}_{\rm g}), \tag{7}$$

where $C_{\rm D}$ is the drag coefficient, which takes the values

$$C_{\rm D} = \begin{cases} 24.\, \mathcal{R}_e^{-1} & \mathcal{R}_e < 1 \\ 24.\, \mathcal{R}_e^{-0.6} & 1 < \mathcal{R}_e \leq 800 \\ 0.44 & \mathcal{R}_e > 800, \end{cases} \tag{8}$$

where $\mathcal{R}_e$ is the Reynolds number of the flow around the planetesimals, defined by

$$\mathcal{R}_e = 2 R_{\rm p} v_{\rm pg} / \nu_{\rm p}, \tag{9}$$

where $v_{\rm pg} = |\boldsymbol{v}_{\rm p} - \boldsymbol{v}_{\rm g}|$, and the molecular viscosity of the flow around the planetesimal is given by

$$\nu_{\rm p} = \lambda c_{\rm s}/3 \tag{10}$$

in most of the global simulations we have performed. It should be noted that in the local simulations, however, the molecular viscosity was defined by

$$\nu_{\rm p} = \lambda c_{\rm s}/2, \tag{11}$$

so we have run one global model (G5) adopting this value. The molecular mean-free path $\lambda = (n\sigma_{\rm H_2})^{-1}$, where $n = \varrho/(\mu m_{\rm H})$ is the number density of particles, μ is the mean molecular weight, and $m_{\rm H}$ is the mass of the hydrogen atom. All but one global simulation adopted the assumption that the disc gas is composed entirely of molecular hydrogen, giving $\mu = 2$. The local shearing box models adopted a value of $\mu = 2.4$, so we have run one global model (G5) using this value in order to provide a direct comparison between local and global models. We adopt a value of $\sigma_{\rm H_2} = 10^{-15}\,{\rm cm}^2$ for the collision cross-section of molecular hydrogen (Rafikov 2004). Trilinear interpolation is used to obtain the gas density and velocity at the position of each planetesimal.

The time integration of the particle motion in the shearing box simulations was performed as follows. Because the gas drag relations are of the form v^α in the relative velocity $v = |v_{\rm g} - v_{\rm p}|$, the update can be performed analytically. In the case $\alpha = 1$, the relevant time-scale ω^{-1} is just the classical stopping time, and the decay is exponential. The update from time t_n to time t_{n+1} with time-step δt can then be written as

$$v_{n+1} = v_n\, {\rm e}^{-\omega\, \delta t}. \tag{12}$$

For $\alpha \neq 1$, we obtain power-law solutions for the damping of the relative velocity, which can be expressed as

$$v_{n+1} = \left[v_n^{1-\alpha}\, (1 + (\alpha - 1)\, \tilde{\omega}\, \delta t) \right]^{\frac{1}{1-\alpha}}\,, \tag{13}$$

where $\tilde{\omega}^{-1}$ is now a generalized 'stopping time' defined by $\tilde{\omega} = f_{\rm dr}\, v^{-1}$, with $f_{\rm dr}$ the specific drag force acting on the particle.

In the global simulations, the particles were evolved using a fifth-order Runge–Kutta scheme (Press et al. 1996).

3 RESULTS

We organize the discussion of our results by first describing the evolution of the disc models. We then describe the evolution of the velocity dispersion (or equivalently eccentricity) of embedded planetesimals, followed by a discussion of their migration through changes in the semimajor axes.

3.1 Hydromagnetic turbulence – local model

Restricting one's consideration to a local approach, one might naïvely think that a relatively small box should suffice to capture the relevant dynamics (see Regev & Umurhan 2008, for a general discussion on limitations of the local approximation). As can be seen in Fig. 2, this notion is supported by looking at the turbulent stresses created by the saturated MHD turbulence. Taken as the only criterion, one arrives at the conclusion that box sizes of $\gtrsim 4H$ are sufficient to study the local stirring of particles – but this is misleading as the gravitational torques acting on the planetesimals are strongly affected by spiral density waves, which arise as a secondary feature of the vigorously driven turbulence in a shearing background.

In a series of two papers, Heinemann & Papaloizou (2009a,b) study the mechanisms by which spiral density waves are excited in a differentially rotating fluid. One important conclusion of their work is that a minimum azimuthal extent $L_y \gtrsim 6H$ is required to properly capture the dynamics of spiral waves. This is exactly what we see when looking at the autocorrelation function (ACF) of the vertically integrated density, as plotted in Fig. 3. Here the thick black line indicates the contour where the correlation falls off to e^{-1}, and we see that density structures are predominantly trailing waves with an azimuthal extent of about six pressure scaleheights. The aspect ratio of the approximate ellipse is about one-sixth, indicating that convergence in the radial direction should be obtained much earlier (cf. right-hand panel of Fig. 8).

Returning to Fig. 2, we see that this requirement is reflected in the relative rms density fluctuations $\langle \delta\varrho/\varrho \rangle$ measured in the saturated turbulent state (uppermost curve in Fig. 2). Increasing the box size from $2H$ to $8H$ results in an increase of ∼75 per cent in the relative rms fluctuations. This is considerably larger than the ∼25 per cent increase found by Yang et al. (2009), who performed a similar study. As the authors themselves mention, even this not particularly dramatic effect seems to strongly affect particle stirring. This can be understood when taking into account the central finding of the simulations undertaken in Heinemann & Papaloizou (2009b), namely that spiral density waves quickly grow into the non-linear regime where they develop steep shock-like features. It seems natural that the resulting intermittent density structure creates highly fluctuating torques, gravitationally enhancing the turbulent velocity dispersion of embedded planetesimals. We examine this issue in more detail in Section 3.3.

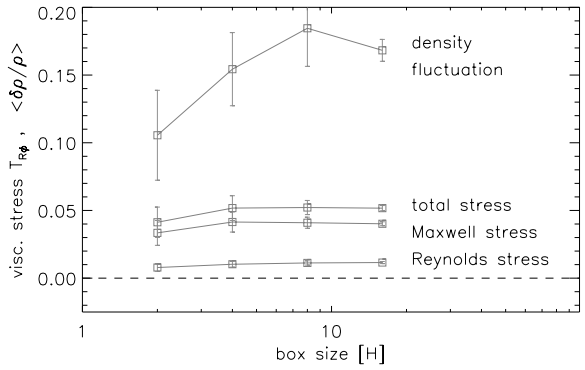

Figure 2. Box size-dependence of key indicators characterizing the hydromagnetic turbulence: while both the Reynolds and Maxwell contributions to the turbulent stress are well converged for azimuthal box sizes above $L_y \gtrsim 4H$, the effected density waves are clearly suppressed in too small boxes. Converged values for the relative density fluctuation can only be obtained for $L_y \gtrsim 8H$. This is directly reflected in the gravitational torques acting on the particles (cf. Fig. 8).

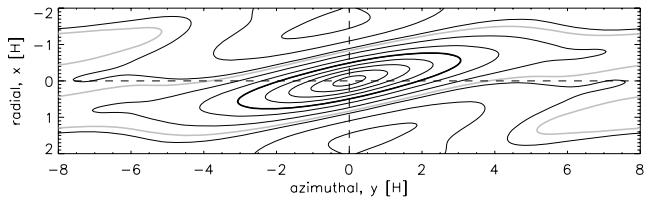

Figure 3. 2D ACF of the vertically integrated gas density, computed from six uncorrelated snapshots of a simulation with box size $4H \times 16H \times 2H$. The thick black contour indicates a value of e^{-1} while the thick grey line marks the first zero-crossing.

3.2 Hydromagnetic turbulence – global models

Prior to inserting the planetesimals in the global disc models, we allow the MRI to develop into quasi-steady non-linear MHD turbulence, with well-defined volume-averaged stresses operating. An example of the time history of the Maxwell, Reynolds and total volume-averaged stress (taken from model G0/G1) is presented in Fig. 4, and the total stress generated in each of the models as a function of time is shown in Fig. 5. It is clear that the models have

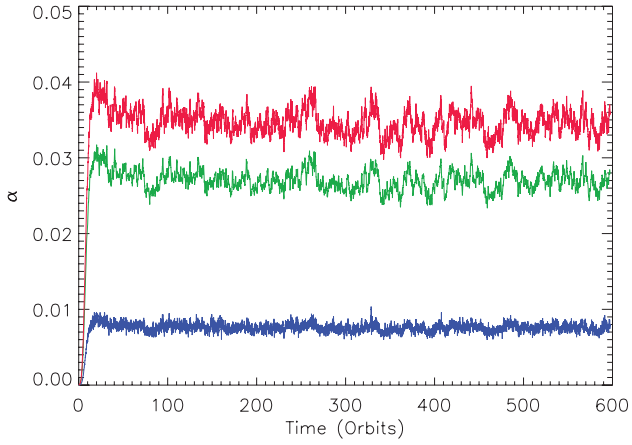

Figure 4. Contributions of the Reynolds (lower) and Maxwell (middle line) stresses to the effective α parameter (upper line) versus time for model G1.

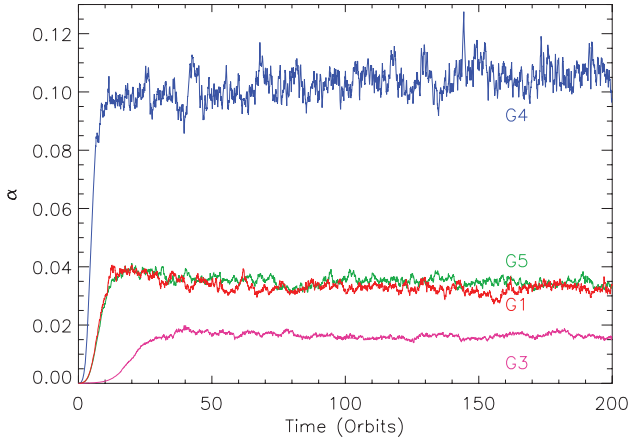

Figure 5. Evolution for the total α value for the models G1, G3, G4 and G5 described in Table 1.

evolved to a quasi-steady state. The turbulence generates a distribution of density and surface density fluctuations which are well fitted by Gaussian distributions. The computed standard deviations for these Gaussian fits (which we denote as $\langle \delta\varrho/\varrho \rangle$ and $\langle \delta\Sigma/\Sigma \rangle$) are tabulated in Table 1 for each disc model, along with the time-averaged stress parameter α. As can be seen from Table 1, our models generate α values in the range $0.017 \leq \alpha \leq 0.101$, with corresponding rms values for $\langle \delta\varrho/\varrho \rangle$ in the range $0.101 \leq \langle \delta\varrho/\varrho \rangle \leq 0.266$.

In terms of physical parameters, the global model which is most similar to the shearing box simulation is run G5. We see that $\alpha \simeq 0.05$ in Fig. 2 for the shearing box simulation, whereas $\alpha = 0.035$ for model G5 because of the differing magnetic field topologies and strengths. The density fluctuations for the shearing box model give $\langle \delta\varrho/\varrho \rangle = 0.17$, whereas $\langle \delta\varrho/\varrho \rangle = 0.13$ for model G5.

In Section 3.1, it was shown that the two-point correlation function for the density field obtained in local shearing box simulations was highly anisotropic, with structure in the azimuthal direction being stretched by a factor of $\sim$6 relative to the radial direction. We plot the corresponding two-point correlation function for model G1 in Fig. 6. It is very similar to that shown in Fig. 3 for the shearing box run, indicating strong similarities in the density structures obtained in local and global simulations.

3.3 Gravitational torques versus shearing box size

To illustrate the strong dependence of the disc gravity on the domain size in local simulations, we performed sets of runs with varying radial and azimuthal extents of the box. As a measure of the magnitude of the stirring, we record time series of gravitational torques at fixed positions and compute the width of the resulting distribution function. This is exemplified in Fig. 7, where we see that, only for large-enough boxes, the torques are consistent with a normal

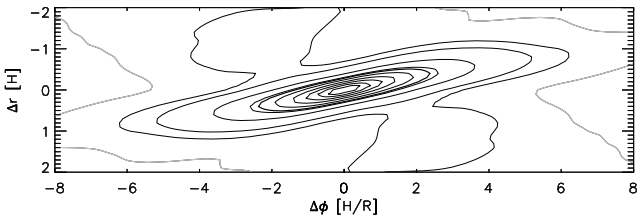

Figure 6. Contours of the two-point correlation of the surface density averaged over six snapshot from model G1. The heavy contours represent the e^{-1}, and the zero level is represented by the grey line.

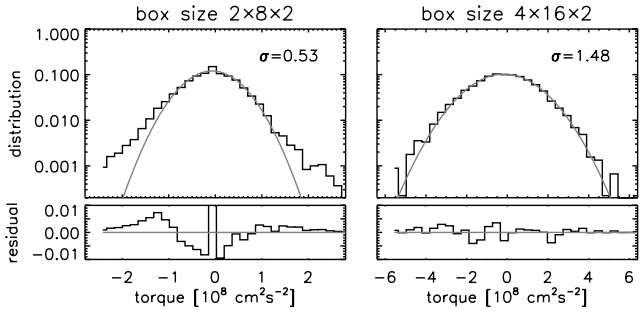

Figure 7. Time-averaged distribution of the gravitational torques acting on a set of particles. Left: small box, the distribution shows excess of both large and small values (as typical for intermittency). Right: large box, the histogram is well represented by a normal distribution centred around zero and with a standard deviation of $1.48 \times 10^8\,\mathrm{cm^2\,s^{-2}}$.

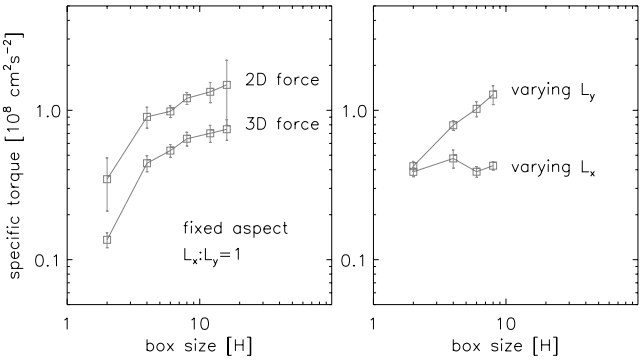

Figure 8. Left: specific gravitational torques versus box size as determined by fitting a normal distribution (cf. Fig. 7). Gravitational torques computed via the column density ('2D force') are consistently enhanced by a factor of roughly 2, as expected from a simple geometric argument. Right: isolation of the effects due to variation in L_x, and L_y, respectively.

distribution. Gaussian fluctuations, in turn, warrant stochastic modelling as considered by Youdin & Lithwick (2007), for example, for the case of interactions via gas drag.

The intermittent distribution seen in the left-hand panel of Fig. 7 is likely related to recurring channel modes and the spiky nature of time series for the turbulent stresses, which occurs when going to too narrow boxes in the radial direction. This phenomenon, which is related to the truncation of the dominant parasitic modes, was first observed by Bodo et al. (2008), and we can confirm this result with our simulations.

As can be seen in the left-hand panel of Fig. 8, the torques show a pronounced dependence on the box size, spanning almost one order of magnitude. Even for $L \gtrsim 8H$, a weak trend towards higher torques is visible, albeit remaining within the error bounds.

As already discussed in Section 2.3, using the column density for computing forces consistently enhances the torques by a constant geometric factor. For a fixed vertical extent L_z, the results can be corrected accordingly.

As expected from the shape of the ACF in Fig. 3 and the arguments given in Heinemann & Papaloizou (2009a), the observed dependence on the box size is primarily a dependence on L_y. This is illustrated in the right-hand panel of Fig. 8, where we plot the respective dependence on L_x and L_y separately.

3.3.1 Torque correlation time

In addition to examining the dependence of gravitational forces on the box size, it is also important to consider the influence of the box size on the correlation time associated with the stochastic gravitational forces experienced by embedded bodies. A key issue here is whether the periodicity of the shearing box, which allows for the possibility of waves in the flow to propagate radially past an embedded planetesimal on multiple occasions prior to damping, combined with advection due to the background shear flow, can modify the recurrence time of the temporally varying gravitational field.

In the previous section, we discussed the value of the standard deviation of the stochastic torques obtained for runs with different box sizes. Using the time series for the stochastic torques obtained from these simulations, we can calculate the ACF for the torques as a function of box parameters. A selection of the ACFs we obtained are plotted in Fig. 9.

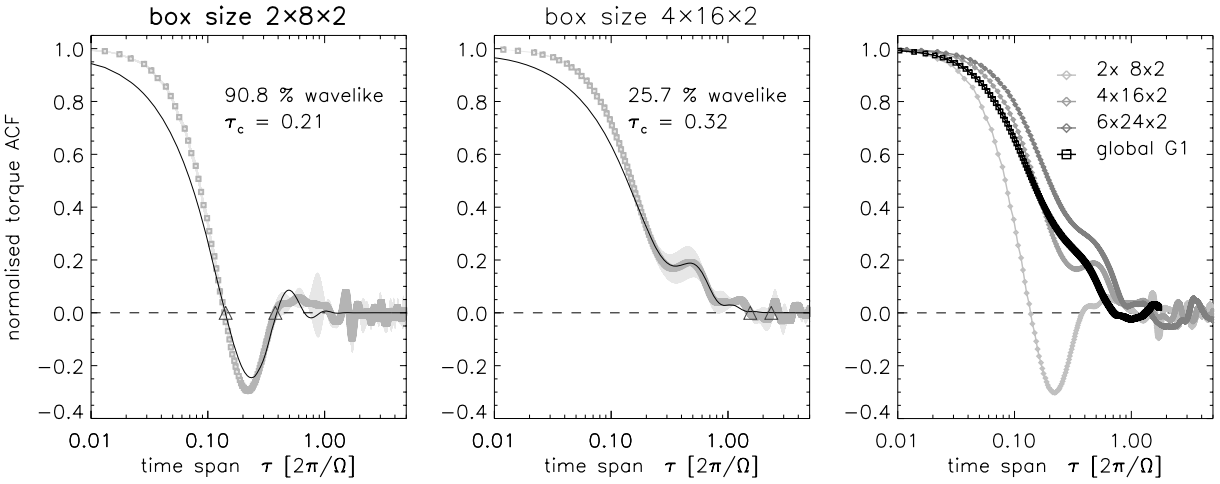

Figure 9. Box size-dependence of the torque autocorrelation. Left and centre: best fits according to equation (14) (solid black line) for a small and large box, respectively. The torque ACFs (dark grey lines) are measured at a fixed position, and error intervals (shaded areas) are estimated from considering sub-intervals in time. The first and second zero-crossing are indicated by triangles. Right: comparison between local models and the global run G1 applying comparable spatial resolution. Excellent agreement is obtained if a large enough box-size is chosen.

In the left-hand panel of Fig. 9, we show the torque ACF for a box with size $2H \times 8H$ in the horizontal direction. The plot can be directly compared to fig. 15 in Yang et al. (2009), and the results are very similar. The position of the first and second zero-crossing and the relative amplitude of the negative part of the ACF are in good agreement. Yang et al. have speculated that the observed undershoot may be responsible for reducing the diffusion coefficient. While this might in fact be the case, we suspect that the observed feature is probably an artefact due to the periodic boundary conditions, limited box size and aspect ratio.

The sinusoidal modulation of the signal in the ACF is consistent with periodicity being introduced into the temporal evolution of the torques caused by density waves traversing the box in the radial direction multiple times before they are dissipated. Looking at animations of the column density, one can identify local density enhancements whenever two waves cross each other. These features, which create strong torques locally, are more pronounced in smaller boxes, and also at higher resolution (where the dissipation time is somewhat enhanced). Studying a set of simulations, we found the dependence on the box size and aspect ratio to be dominant, while the trend with resolution is rather weak (∼30 per cent when increasing the resolution by a factor of 3) – we hence focus on this issue. To pursue a more quantitative analysis, we fit the computed ACFs with the following model:

$$S_\Gamma(\tau) = [(1-a) + a\,\cos(2\pi\,\omega\,\tau)]\;\mathrm{e}^{-\tau/\tau_c}\,, \qquad (14)$$

with three free parameters, namely a, indicating the relative strength of the proposed sinusoidal feature, ω giving its period, and finally the correlation time τ_c, assumed to be common between the two components.

For the sake of simplicity, we assume that there exists only one wave-like mode and both components of the mix decay with the same characteristic time. While more elaborate fits (e.g. with separate decay times) produce slightly better agreement, we found no systematic trend in this dependence. We therefore refrain from the associated further complication.

As one can see in the left-hand and centre panels of Fig. 9, the model produces reasonable fits for the given data. For the small and large boxes, we infer relative amplitudes of the cosine-like feature of ∼90 and ∼25 per cent, respectively. This illustrates the trend with box size at a fixed aspect ratio. Contrary to our own expectation, the periodicity is not simply related to the *radial* extent of the box. This has been found studying a set of simulations, keeping $L_y = 8H$ fixed and progressively increasing L_x. Even at $L_x = 16H$, the ACF remains unchanged and is very similar to the one in the left-hand panel of Fig. 9. It appears instead that changing both the box size *and* aspect ratio leads to changes in the torque correlation time, as illustrated in the centre panel of Fig. 9 for a run with box dimensions $4H \times 16H \times 2H$. The implication appears to be that the periodicity introduced into the run of torques versus time, and hence into the ACF, results from a combination of wave propagation in radius and advection in the azimuthal direction due to the background shear.

Having identified a periodic feature, we can now make an unbiased estimation of the temporal correlation of the fluctuating torques. Although unexpected from a naïve by-eye inspection, the correlation times in the two cases only differ by about 50 per cent. This shows that estimating the correlation time according to location of the first zero crossing when the ACF has a significant sinusoidal component can be misleading. We suggest that as an alternative the correlation time be estimated using a fitting formula such as given in equation (14). We see from the central panel of Fig. 9 that $\tau_c = 0.32$ for our large shearing box model.

Finally, in the right-hand panel of Fig. 9, we compare the torque ACFs of our global simulation G1 with local simulations at comparable resolution. We see that excellent agreement is obtained when using large-enough boxes with an elongated aspect ratio, indicating that the correlation time for the global simulation G1 $\tau_c \simeq 0.32$. Interestingly, the correlation time measured from the zero crossing point for model G1 is $\tau_c = 0.68$, about a factor of 2 larger than we infer from the fitting procedure described above.

In order to check the sensitivity of model G1 to numerical resolution, we have re-run it at both double and quadruple resolutions in the radial and azimuthal directions, giving ($N_r \times N_\phi$) equivalent to (320×2560) and (640×5120), respectively, for a disc which covers the full 2π in azimuth. These runs have 20 and 40 cells per mean scaleheight in the radial and azimuthal directions. The ACFs measured in each of these runs are very similar to that shown in the right-hand panel of Fig. 9.

3.4 Gravitational stirring versus distance in global models

As described in Section 3.2, the disc models listed in Table 1 were evolved until they had reached a statistical steady state, prior to inserting the planetesimals. Before discussing the evolution of planetesimals which experience gas drag, we examine the length-scales over which gravitational stirring of planetesimals by the turbulent disc occurs.

We performed a series of simulations using the disc model G0, where we defined a gravitational sphere of influence of varying size, $R_{\rm cut}$, around the planetesimals (which do not experience the gas drag force in this particular simulation). We then examined how the radius of this sphere of influence changed the evolution of the planetesimal velocity dispersion. The sphere of influence in each simulation is defined by a radius, $R_{\rm cut}$, measured in units of the local value of H. Gas within this sphere of influence exerts a gravitational force on the planetesimal. At the edge of this sphere, the contribution to the force is tapered to zero over a distance equal to H using the hyperbolic tangent function. For example, a sphere of influence equal to $R_{\rm cut} = 2H$ allows a full contribution to the disc force within $1H$, and beyond this the force contribution is tapered to zero.

Fig. 10 shows the evolution of the rms of the radial velocity dispersion, $\sigma(v_{\rm r})$, as a function of $R_{\rm cut}$, where $\sigma(v_{\rm r})$ is measured in units of the sound speed. For this model, $c_{\rm s} = 666\,{\rm m\,s^{-1}}$ at $r = 2.5$ (5 au). It is clear that contributions to the gravitational force occur even beyond a cut-off radius $R_{\rm cut} = 8H$, in agreement with the calculations presented in Section 3.3 for shearing boxes of different size. The basic reason for this has already been explained: spiral waves generated by the turbulence provide coherent structures which are stretched in the azimuthal direction by the shear, and contribute significantly to the stochastic gravitational forcing experienced by the planetesimals. Clearly, computational domains are required which are large enough to capture the gravitational stirring which occurs on scales up to 8–10 scaleheights, at least in the azimuthal direction.

Examining the curve in Fig. 10 which corresponds to no cut-off in the gravitational force, we see that the evolution of $\sigma(v_{\rm r})$ can be reasonably well fitted as a random walk. The smooth solid line, and the dashed lines, corresponds to the function $C_\sigma \sqrt{t - t_0}$, with $C_\sigma = (8 \pm 0.8) \times 10^{-3}$, where the time is measured in orbits at $r = 2.5$ (5 au).

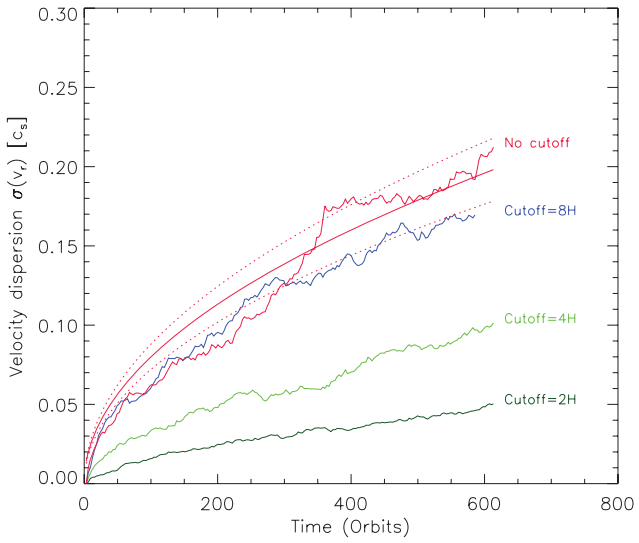

Figure 10. Evolution of the radial velocity dispersion, $\sigma(v_{\rm r})$, in units of the local sound speed, as a function of the size of the gravitational sphere of influence described in the text.

3.5 Evolution of the planetesimal velocity dispersion – local model

After $t_0 = 20$ orbits, when the turbulence driven by the MRI has reached a quasi-steady-state, we disperse several swarms of test particles into the flow. For easy reference, we label these sets as 'G' for the particles that experience the gas gravity only, 'D' for particles subject to the gas drag-force, 'G+D' for the combined effect and 'T' for massless tracer particles. While the sets G and T consist of only one species, the sets D and G+D are composed of 10 species each. Particle radii are $R = 1$ m, 2 m, 5 m, 10 m, 20 m, 50 m, 0.1 km, 0.2 km, 0.5 km and 1 km, respectively. Eight particles are used to represent each size. Due to the low number of particles, we expect sampling errors of the order of 20–35 per cent. In reality, these numbers have to be seen as upper limits. Because our fits are based on time histories, the effective statistical basis is probably somewhat larger than for any given instant in time. To roughly quantify the uncertainty due to Poisson fluctuations, we performed a lower resolved fiducial run with 100 particles for the gravity-only set. Taking 12 subsets of eight particles each, we arrive at a standard deviation of 23 per cent amongst the different realisations. For six sets of 16 particles, this number is only slightly reduced to 18 per cent, justifying the initial choice.

Depending on the particle size and the prevailing form of the coupling, the time evolution of the various species is quite diverse. Massless tracers and small particles with $R_{\rm p} \lesssim 10$ m, whose dynamics are largely controlled by gas drag, essentially follow the turbulent flow and describe a random walk. The larger G+D particles, as well as the G set, are coupled more weakly. For them the orbital dynamics due to the Coriolis and tidal forces become increasingly relevant. Viewed from a local perspective, the motion of these particles can be described as epicyclic oscillations with a modulated amplitude and a stochastically migrating guiding centre, as seen in Fig. 11. Thus, the relevant properties of the particles' motion can be described using two characteristic quantities: (i) orbital eccentricity, or the amplitude of the epicyclic motion (or equivalently the velocity dispersion relative to a circular Keplerian orbit) and (ii) semimajor axis – the position of the guiding centre, which evolves as a random walk as the particles migrate from their

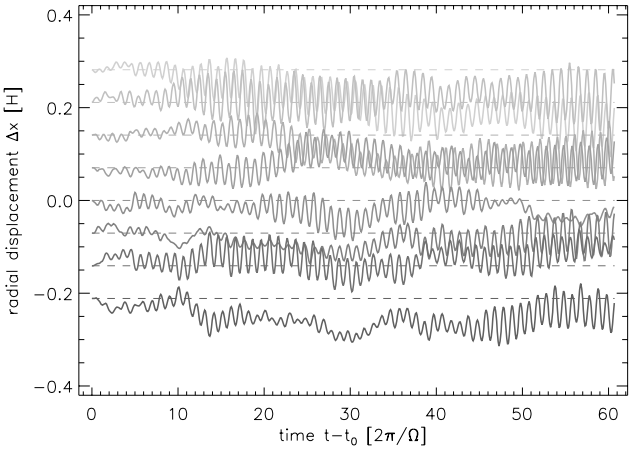

Figure 11. Exemplified temporal evolution of the radial displacement Δx for a swarm of eight gravitationally excited particles. The initial positions have been off-set for clarity as indicated by the dashed lines.

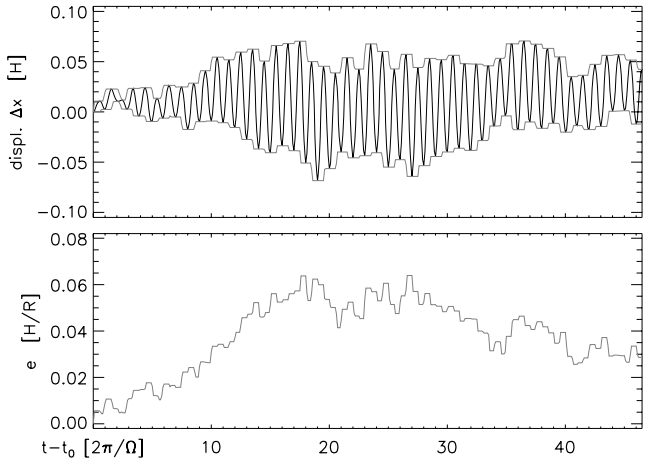

Figure 12. Illustration of the algorithm used to measure the eccentricity (lower panel) of a particle moving on epicyclic orbits via tracking the aphelion and perihelion (upper panel).

initial locations. In this section we examine the eccentricity/velocity dispersion, and consider the migration in Sections 3.7 and 3.8.2.

To separate the stochastic motion of the guiding centre from the epicyclic oscillation, we box car-average the velocity applying a filter-scale equivalent of the orbital frequency. We compute the eccentricity of the particle's orbit by tracing the position of the aphelion and perihelion, respectively. From these, we compute

$$k = \frac{R_0 + x_{\rm apo}}{R_0 + x_{\rm per}} \qquad \text{and} \qquad e = \frac{k-1}{k+1}, \tag{15}$$

with $R_0 = 5\,$au the location of our local box. The tracking of the extrema and the resulting eccentricity function are illustrated in Fig. 12, where we see that $e(t)$ itself follows a random walk. This means that gravitational stirring can both excite and damp the epicyclic motions of individual particles. As we will see shortly, however, the influence of the stochastic forcing on the ensemble of planetesimals will increase the rms eccentricity amongst the members, and therefore heat-up the ensemble as a whole.

3.5.1 Saturation amplitudes

Needless to say that the velocity fluctuations will not grow *ad infinitum*, but will reach a saturated state once the aerodynamic damping reaches the level of the stochastic forcing. This is illustrated in Figs 13 and 14, where we plot the temporal evolution of the radial velocity dispersions for large and small bodies, respectively.

Looking at the lowermost curves in Fig. 13, we see that the random velocity of particles with $50\,{\rm m} \gtrsim R_{\rm p} \gtrsim 200\,{\rm m}$ saturates on time-scales of several hundred orbits. In this regime, the saturation amplitude increases with the particle size, reflecting the weaker damping for larger bodies. Because the gravitational stirring is independent of the particle mass, smaller bodies reach their saturated state earlier compared to heavier ones. For larger bodies (500 m, 1 km), we do not achieve equilibrium, but after 500 orbits we note that $\sigma(v_{\rm r}) \simeq 0.08 c_{\rm s}$ for 1km-sized bodies (where $c_{\rm s} = 1\,{\rm km\,s^{-1}}$ in this model).

Unlike for their larger counterparts, smaller bodies are predominantly affected by gas drag and we observe the opposite trend with respect to the saturation amplitudes (see Fig. 14). At first, it seems surprising that $\sigma(v_x)$ can be excited beyond the turbulent velocity $v_{\rm rms} = 0.13\,c_{\rm s}$ of the gas. This is, however, only the case for the radial velocity and can be understood from the orbital dynamics

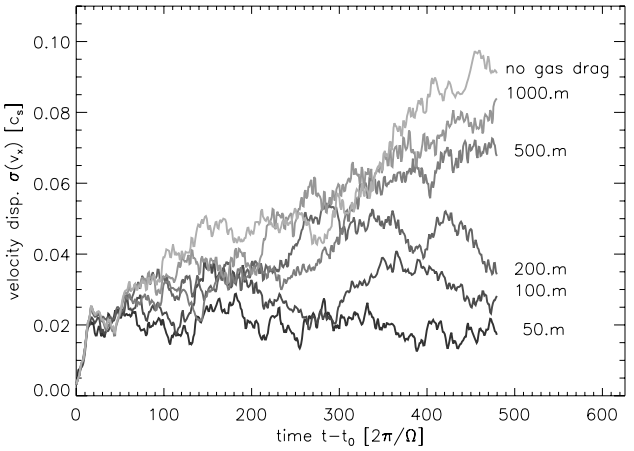

Figure 13. Evolution of the radial velocity dispersion for set 'G+D'. For sizes above $R \gtrsim 1\,$km, forces due to gas drag become gradually negligible and the evolution is described by a $\sqrt{t}$ behaviour.

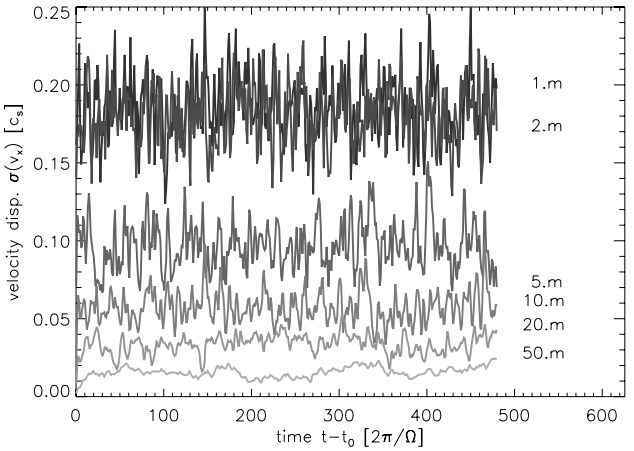

Figure 14. Same as Fig. 13, but for smaller particles, subject only to gas drag. Note the opposite trend with particle radius (also cf. Fig. 15 below).

which leads to $\langle v_x \rangle \approx 2\langle v_y \rangle$ as characteristic of epicycles (also cf. fig. 5 in Youdin & Lithwick 2007).

The saturation amplitudes in the velocity dispersion which arise as a function of particle size are compiled in Fig. 15. With the exception of the $R_{\rm p} = 1\,$m species, which is tightly coupled to the gas, $\sigma_{\rm s}(v_x) \approx 2\,\sigma_{\rm s}(v_y)$ as expected from orbital dynamics. The results for set D can be readily compared to the upper panel[3] of fig. 5 in Youdin & Lithwick (2007), which shows saturation amplitudes obtained from a simple turbulence model. Considering the vast differences in the two approaches, the results agree surprisingly well.

Considering the G+D set, the particle rms velocity takes its maximum for $\tau_{\rm s} \lesssim 1$ and falls-off to about 10 per cent its peak value at $\tau_{\rm s} \simeq 10^3\,\Omega^{-1}$. This is a somewhat shallower decline than in the model of Youdin & Lithwick, where this value is reached at 10^2 already. The minimum radial velocity dispersion obtained is $\simeq 0.1 v_{\rm rms}$ (where $v_{\rm rms}$ is the turbulent velocity dispersion of the gas). This minimum value marks the point where the G+D set deviates from the D set (see RHS in Fig. 15). This implies that objects of size $\approx$50 m enjoy the relative comfort of being the least affected by their

[3] As we will discuss in Section 3.8.2, we find a characteristic eddy time $\tau_{\rm e} \approx \Omega^{-1}$ in our simulations such that the standard case applies.

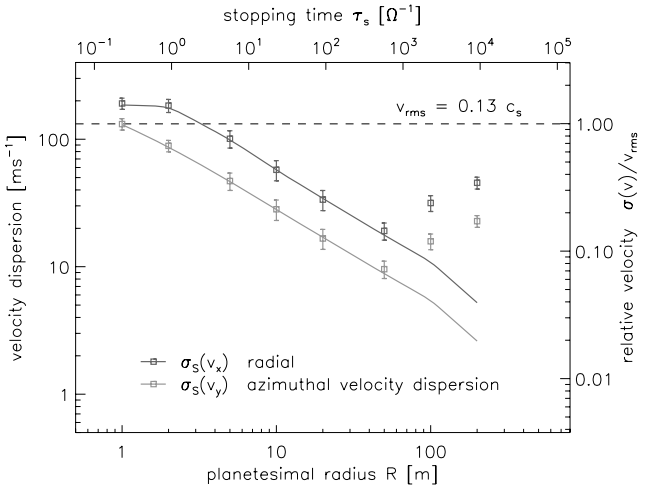

Figure 15. Saturated velocity dispersions as a function of planetesimal radius, R_p, and stopping time, τ_s, respectively. Particles which feel both the gas gravity and drag force (*symbols*) deviate from the ones that only feel the gas drag (solid lines) for sizes larger than $R \approx 50$ m.

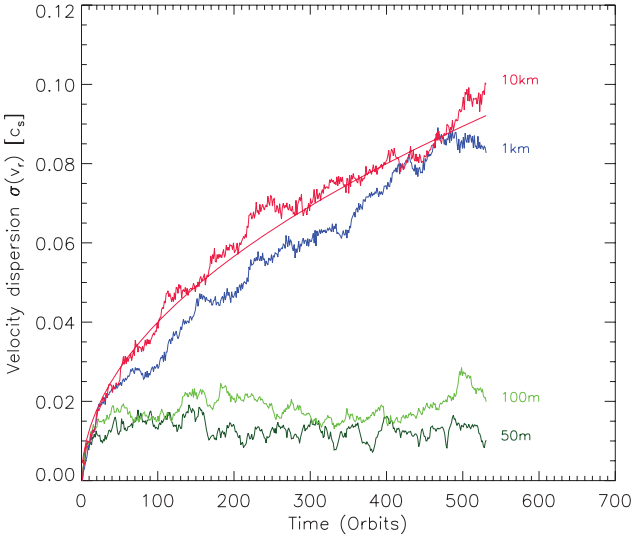

Figure 16. Evolution of the radial velocity dispersion, $\sigma(v_r)$, in units of the sound speed, for planetesimals of different size from run G5.

turbulent surroundings, with a velocity dispersion that corresponds to 15–20 m s^{-1}. Interestingly this is close to the speeds required for catastrophic break-up of planetesimals in the 10–100 m range (Benz & Asphaug 1999; Stewart & Leinhardt 2009).

For larger sizes, the velocity dispersion is seen to rise as the particle size rises in Fig. 15, but the largest bodies we consider have not had time to reach the equilibrium values of their velocity dispersion. The explanation for the existence of the minimum velocity dispersion observed in Fig. 15 is straightforward. Smaller bodies are tightly coupled to the gas, and so attain a velocity dispersion close to that of the gas itself. Larger particles experience a significantly smaller gas drag, which then contributes weakly to counterbalancing the stirring effect of the stochastic gravitational force provided by the disc, leading to a large velocity dispersion. Intermediate-sized particles in the 50–100 m range are sufficiently decoupled from the gas that they experience an orbit-averaged drag force that causes significant damping of the eccentricity growth driven by the disc gravity.

3.6 Evolution of the planetesimal velocity dispersion – global model

We now examine the evolution of the velocity dispersion of planetesimals of different size which experience the gas drag force within global models, focusing on the radial component of this quantity. The key issues that we explore are the magnitude of the velocity dispersion attained as a function of planetesimal size and disc model parameters, and the implications for the outcomes of collisions between planetesimals for the growth of planets.

3.6.1 Model G5 – comparing local and global models

The global disc model with physical parameters most similar to the shearing box simulation is model G5. As described in Section 2.4, the shearing box model adopted $H = 0.075$, and used equation (11) and $\mu = 2.4$ in defining the strength of the gas drag force. Most of the global simulations adopted model parameters which are slightly different from these, a fact which was discovered after most of the simulations presented here had been completed. We present here, however, a global model with the same parameters used in the shearing box run for the purpose of providing a direct comparison. The only difference in the underlying disc models is the choice of magnetic field topology and strength, with the resulting α values being $\alpha \simeq 0.05$ for the shearing box and $\alpha \simeq 0.035$ for the global model, which are similar enough for a meaningful comparison to be made. The planetesimal sizes considered in this run were 10 m, 20 m, 50 m, 100 m, 1 km and 10 km, with each size being represented by 25 particles.

The evolution of the radial velocity dispersion, expressed in units of the local sound speed, is shown in Fig. 16 for planetesimals with sizes in the range 50 m–10 km. Comparison with Fig. 13, which shows the same data for the shearing box simulation, indicates that there is good agreement between the two simulations. The 50 m and 100 m sized objects quickly attain equilibrium values for $\sigma(v_r)$ in the range 0.01–0.02c_s (where $c_s = 1$ km s^{-1} for this model), similar to the values obtained in the shearing box run. After 500 orbits $\sigma(v_r) \simeq 0.08 c_s$ for the 1 km sized bodies, and the 10 km bodies have $\sigma(v_r) \simeq 0.1 c_s$, again in good agreement with the shearing box results.

In principle, we would expect the shearing box simulations to generate slightly larger velocity dispersions, due to the more vigorous turbulence exhibited by that model, and the correspondingly larger value of $\langle \delta\varrho/\varrho \rangle$. The fact that the gravitational stirring is actually found to be very similar is probably because the global simulations allow for a faster growth of the velocity dispersion due to larger length-scales being included in the disc gravity force calculation. More distant density perturbations are thus able to contribute to the stochastic gravitational field experienced by the planetesimals, providing a small boost to the gravitational stirring.

Whereas the larger planetesimals have not achieved an equilibrium value for $\sigma(v_r)$ by the end of the simulation, planetesimals with sizes in the range 10–100 m have. We plot the saturated value of $\sigma(v_r)$ as a function of particle size in Fig. 17, and in agreement with the results obtained for the shearing box simulation, we observe that there is a minimum value for $\sigma(v_r)$ for bodies of size $\simeq$50 m, corresponding to $\sigma(v_r) \simeq 20$ m s^{-1}.

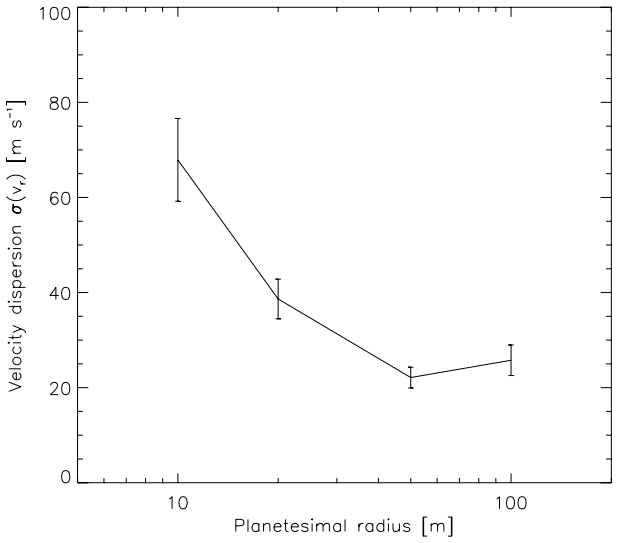

Figure 17. Saturated values of $\sigma(v_r)$, measured in metres per second, as a function of particle size from run G5.

3.6.2 *Evolution as a function of α: models G1–G4*

We now consider the evolution of the velocity dispersion as a function of the turbulent strength, as measured by α, by presenting the results from models G1, G2, G3 and G4. As shown in Table 1, the value of α was modified by changing the strength of the net toroidal magnetic field in the initial conditions. Models G1 and G2 differed only in the size of their azimuthal domains ($\pi/2$ for G1 and 2π for G2), but the increase in domain size for G2 causes a small increase in α (presumably due to the presence of low-order MRI modes). We note that the disc parameters and values used in computing the gas drag strength were different in these models compared with run G5, and so these runs are not directly comparable with that one.

The evolution of $\sigma(v_r)$ for models G1–G4 is presented in Fig. 18 for planetesimals of size 10 m, 100 m, 1 km and 10 km. Overall, the evolution of $\sigma(v_r)$ is found to be a weak function of α [we find an approximate scaling $\sigma(v_r) \propto \alpha^{0.20}$; see below], and the evolution of $\sigma(v_r)$ for models G1 and G2 is in good agreement. Although α (and $\langle \delta\Sigma/\Sigma \rangle$) is larger in model G2, we find that the velocity dispersion increases at a slightly slower rate for the larger planetesimals than found in model G1. The difference, however, is well within the $\sqrt{N}$ variations expected for the low numbers of particles used.

In comparison with run G1, G3 shows slower growth of $\sigma(v_r)$ for the larger planetesimals, and a smaller saturated value of $\sigma(v_r)$ for the 10 m sized bodies, as expected given the smaller value of α. Run G4 shows correspondingly faster growth, and larger saturated values, of $\sigma(v_r)$ due to the larger value of α. Each of the plots in Fig. 18 shows fits to the data for the 10 km bodies, assuming a functional form $\sigma(v_r) = C_\sigma(v_r)\sqrt{t}$. The values of $C_\sigma(v_r)$ for each model are tabulated in Table 1. Fitting the data for α and $C_\sigma(v_r)$ listed in Table 1, using an expression of the form $C_\sigma(v_r) = K_{v_r}\alpha^q$, leads to a best-fitting solution with $q = 0.20$ and $K_{v_r} = 1.64 \times 10^{-2}$. We use this fit to the data in Section 3.6.4, where we discuss the expected saturation value of $\sigma(v_r)$ for 1 km and 10 km sized planetesimals as a function of α.

3.6.3 *Saturation values of σ(v_r) for 1 km and 10 km planetesimals*

Our simulations have not run for sufficient time for $\sigma(v_r)$ to reach its equilibrium value for the 1 km and 10 km sized bodies. Assuming that saturation is reached when the stochastic gravitational forcing is balanced by gas drag damping, we can estimate the saturation values by equating the forcing and damping time-scales. Working in terms of the orbital eccentricity [where $e \simeq v_{\rm disp}/v_{\rm K}$, with $v_{\rm disp} \equiv \sigma(v_r)$ and $v_{\rm K}$ being the Keplerian velocity], and using the expression $v_{\rm disp} = C_{v_r}\sqrt{t}$ we can write

$$\tau_{\rm grow} = \frac{e}{{\rm d}e/{\rm d}t} = \frac{2e^2 v_{\rm K}^2}{C_\sigma(v_r)^2}, \tag{16}$$

where $\tau_{\rm grow}$ is the eccentricity growth time. The damping time for the velocity dispersion can be estimated simply from the ratio of the momentum associated with the velocity dispersion and the gas drag force (Ida et al. 2008)

$$\tau_{\rm damp} = \frac{2m_{\rm p} v_{\rm disp}}{C_{\rm D}\pi R_{\rm p}^2 \varrho v_{\rm disp}^2}. \tag{17}$$

Equating expressions (16) and (17), and writing the planetesimal mass in terms of its radius and internal density, $\varrho_{\rm p}$, leads to the following expression for the equilibrium velocity dispersion

$$v_{\rm disp} = \left[\frac{4\varrho_{\rm p} R_{\rm p} C_\sigma(v_r)^2}{3C_{\rm D}\varrho}\right]^{1/3}. \tag{18}$$

Noting that $c_{\rm s} = 666\,{\rm m\,s^{-1}}$ at 5 au in our global disc models G1–G4, and expressing $C_\sigma(v_r)$ in SI units, we obtain $C_{v_r} = 3.15 \times 10^{-4}$ for model G1. This leads to estimates of the equilibrium velocity dispersion of $v_{\rm disp} = 765\,{\rm m\,s^{-1}}$ for 10 km bodies (approximately the sound speed), and $v_{\rm disp} = 356\,{\rm m\,s^{-1}}$ for 1 km bodies with $\varrho_{\rm p} = 3\,{\rm g\,cm^{-3}}$ at 5 au in a disc with $\Sigma = 150\,{\rm g\,cm^{-2}}$ and $H/r = 0.05$. These values are clearly very much in excess of the velocities required for catastrophic disruption of 1 km and 10 km sized planetesimals, being many times larger than the escape velocities, $v_{\rm esc}$, from these bodies ($v_{\rm esc} \simeq 12\ {\rm m\ s^{-1}}$ for a 10 km body with $\varrho_{\rm p} = 3\,{\rm g\,cm^{-3}}$). Extrapolating forward in time, the time required to reach the equilibrium value for $v_{\rm disp}$ for the $R_{\rm p} = 10$ km planetesimals is $\simeq 1.75 \times 10^5$ yr, comparable to the runaway growth time-scale at 5 au.

3.6.4 *Saturation of σ(v_r) as a function of α*

Using the expression $C_\sigma(v_r) = K_{v_r}\alpha^{0.20}$ discussed in Section 3.6.2, in conjunction with equation (18), we can estimate the value of α which leads to a particular value of $v_{\rm disp}$ for a particular size of planetesimal

$$v_{\rm disp} = \left(\frac{4\varrho_{\rm p} R_{\rm p} K_{v_r}^2 \alpha^{0.4}}{3C_{\rm D}\varrho}\right)^{1/3}. \tag{19}$$

Using the results from model G1, and working in SI units, we obtain $K_{v_r} = 6.16 \times 10^{-4}$. Values of $v_{\rm disp}$ as a function of α are plotted in Fig. 19 for planetesimal sizes 1 km and 10 km, and for planetesimal internal densities $\varrho_{\rm p} = 1$ and $3\,{\rm g\,cm^{-3}}$. It is clear that even with a small value of $\alpha = 10^{-6}$, equilibrium velocity dispersions are in the range $60 \leq v_{\rm disp} \leq 110\,{\rm m\,s^{-1}}$, somewhat larger than the escape velocities and catastrophic disruption velocities of these bodies. Evidently a protoplanetary disc needs to be very quiescent near its midplane in order to allow for runaway growth to proceed, and to prevent the catastrophic breakup of colliding planetesimals in the 1–10 km size range.

There are obviously a number of caveats contained within the simple arguments presented above. In a disc in which the density is vertically stratified (with or without a dead zone), the dependence of $v_{\rm disp}$ on α may be steeper if the stochastic forcing of planetesimals depends on the magnitude of local density rather than surface density perturbations. It is also possible that mass accretion through

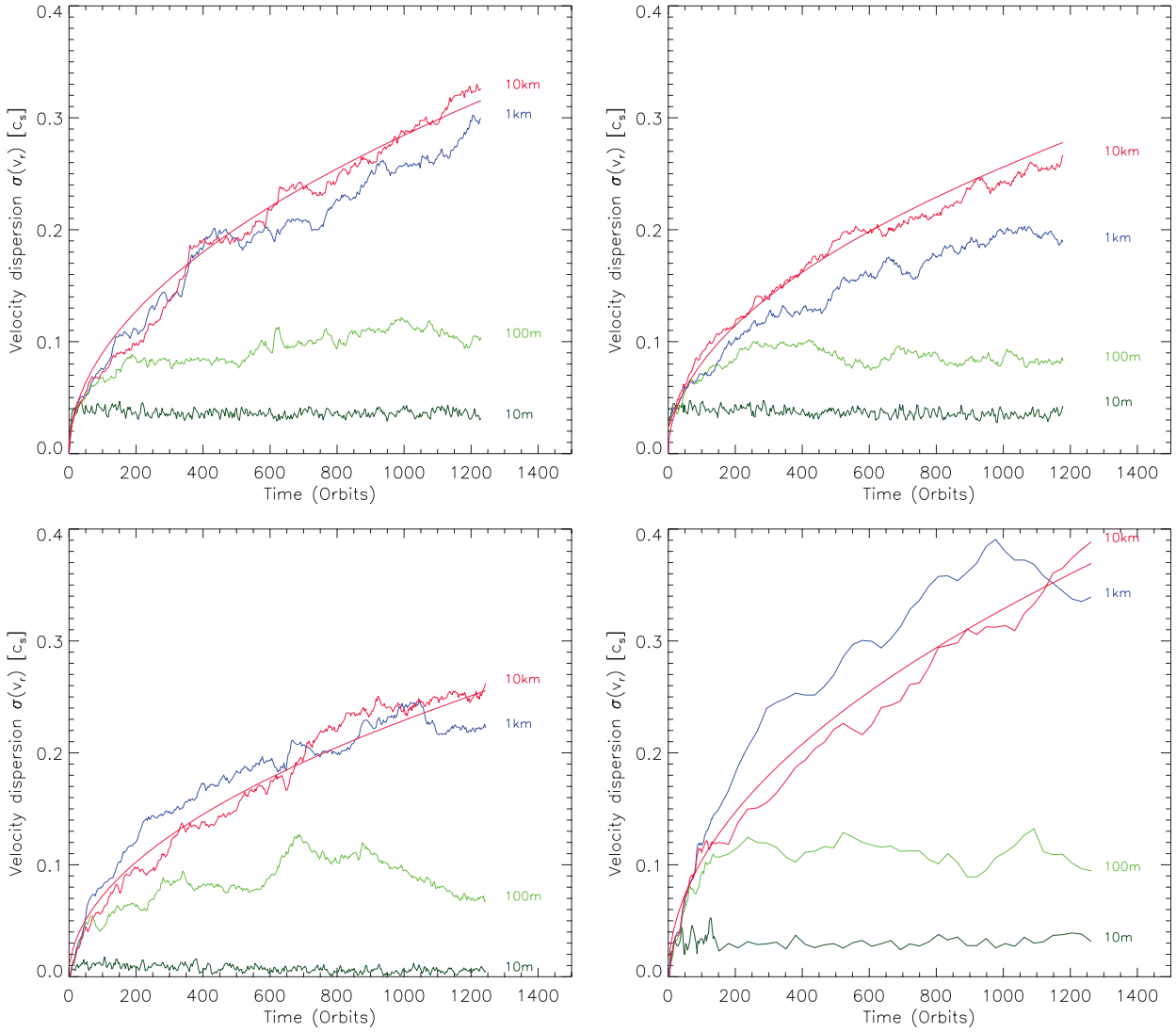

Figure 18. Evolution of the radial velocity dispersion, $\sigma(v_r)$, in units of the local sound speed, for planetesimals of different size from runs G1 (top-left panel), G2 (top-right panel), G3 (lower-left panel) and G4 (lower-right panel). Each panel also displays a fit to the random walk behaviour, as described in the text.

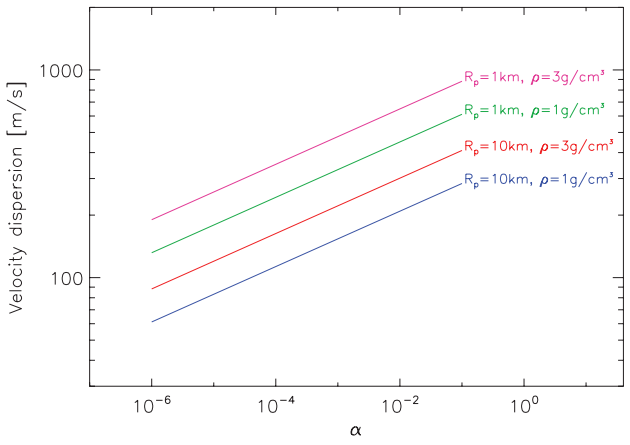

Figure 19. Variation of the saturated velocity dispersion as a function of the turbulent α and the planetesimal density.

the disc may be generated by the winding up of net radial fields in a disc with a dead zone (Turner & Sano 2008), breaking the link between α and $\langle \delta\varrho/\varrho \rangle$, which the above arguments rely upon. Confirmation of the result obtained above will be sought in a forthcoming paper in which we examine planetesimal dynamics in vertically stratified discs with dead zones.

3.7 Radial migration of planetesimals – global models

We now consider the radial drift of the planetesimals, arising both from the effects of gas drag and from the action of the stochastic gravitational torques. The radial drift of large planetesimals is potentially an important effect during planet formation, as it may lead to the delivery of material to regions which have suffered from depletion, and may also enhance the delivery of volatiles to the inner system from beyond the snowline. Radial drift due to gas drag is not present in the local shearing box simulations, since there is no radial pressure gradient to generate sub-Keplerian velocities in the gas. We therefore begin our discussion by examining the results of the global simulations.

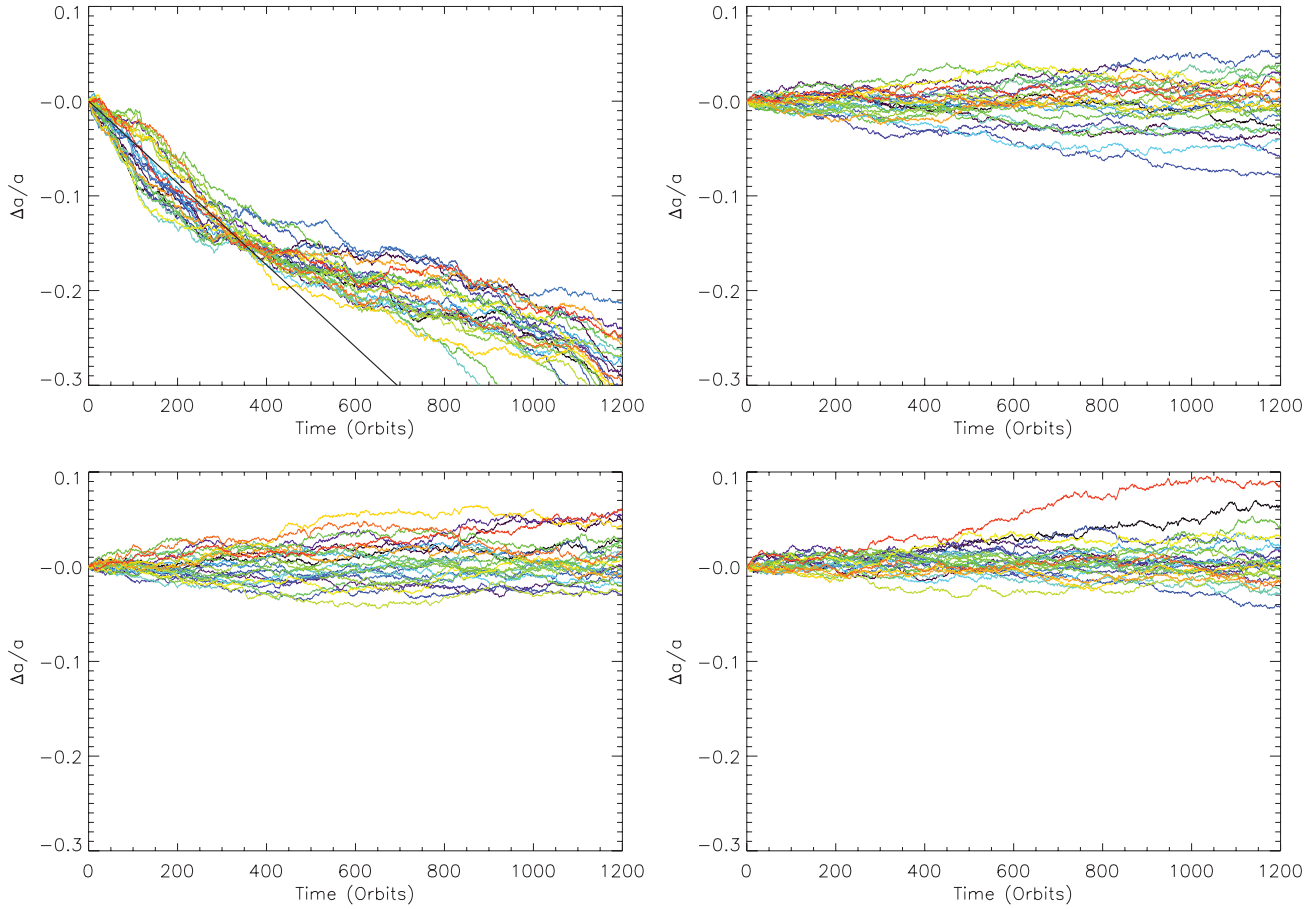

Figure 20. Evolution of the semimajor axis for all planetesimals in run G1. The top-left panel displays data for the 10 m planetesimals, along with the theoretically expected drift within a laminar disc (solid black line). The top-right panel corresponds to the 100 m planetesimals. The lower-left panel refers to the 1 km planetesimals, and the lower-right panel shows the 10 km bodies.

In a sub-Keplerian disc, the gas drag force given by equation (7) will lead to a loss of angular momentum and radial drift of planetesimals at a rate which depends on their size (Weidenschilling 1977). The time over which the gas drag removes an amount of specific angular momentum equal to Δj from an embedded planetesimal is given by

$$\tau_{\rm drag} = \frac{8R_{\rm p}\varrho_{\rm p}}{3C_{\rm D}\varrho}\frac{\Delta j}{r_{\rm p}v_{pg}^2}, \tag{20}$$

where $\varrho_{\rm p}$ is the density of the planetesimal material (here assumed to be 3 g cm^{-3}). Superposed on this inward drift are the stochastic torques experienced by the planetesimals in a turbulent disc, which will cause diffusion of planetesimal semimajor axes (as well as contributing to the eccentricity evolution). The effective diffusion coefficient associated with the diffusion of planetesimal angular momenta can be approximated by $D_j = \sigma_{\rm T}^2\tau_{\rm corr}$, where $\sigma_{\rm T}$ is the standard deviation of the distribution of torques (assuming Gaussian statistics), and $\tau_{\rm corr}$ is the correlation time associated with the stochastic torques (Johnson et al. 2006). The time-scale over which diffusion will change the specific angular momentum of a typical planetesimal by an amount equal to Δj is

$$\tau_{\rm diff} = \frac{(\Delta j)^2}{D_j}. \tag{21}$$

We expect that the effects of radial drift and diffusion will be comparable when equations (20) and (21) are equal, and this is the time-scale over which the drag-induced inward drift of planetesimals of size $R_{\rm p}$ should just become apparent against the isotropic diffusion generated by the turbulence. The random walk associated with the stochastic torques means that the planetesimal size, $R_{\rm p}$, for which inward drift just becomes apparent depends on the magnitude of the change of angular momentum, Δj. Larger values of Δj imply longer evolution times, such that the net inward drift of larger planetesimals, which are increasingly impervious to gas drag, eventually becomes apparent.

Results from model G1 are shown in Fig. 20, which shows the relative change in semimajor axis versus time for all planetesimals, and it is clear that the $R_{\rm p} = 10$ m bodies undergo gas drag-induced inward migration, whereas the larger bodies are dominated by stochastic migration. The rms relative change in semimajor axis, $\sigma(\Delta a/a)$, for the $R_{\rm p} = 10$ km planetesimals is shown in Fig. 21.

Small changes to the specific angular momentum and semimajor axis of a body are related according to

$$\frac{\Delta j}{j} = \frac{1}{2}\frac{\Delta a}{a}. \tag{22}$$

Using equations (21) and (22), we can estimate how far we expect large planetesimals to have diffused in semimajor axis during the 1200 orbits of run time in model G1. The distribution of torques, averaged over all 10 km sized planetesimals, is presented in Fig. 22, and the standard deviation of this torque distribution is found to be $\sigma_{\rm T} = 1.5 \times 10^8$ cm^2 s^{-2} (equivalent to 3.46×10^{-5} in code

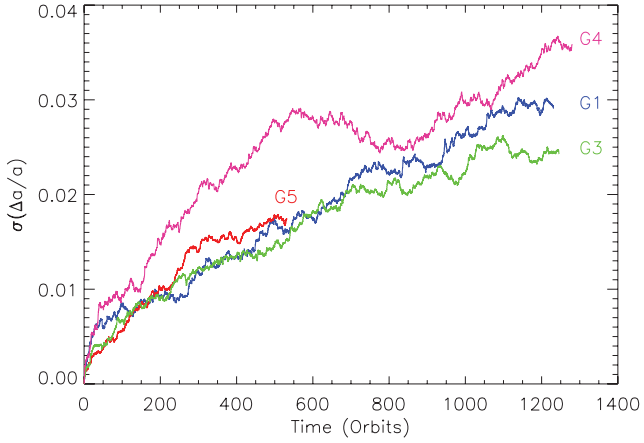

Figure 21. Evolution of the rms change in semimajor axis for 10 km sized planetesimals, where each line is annotated with the run label.

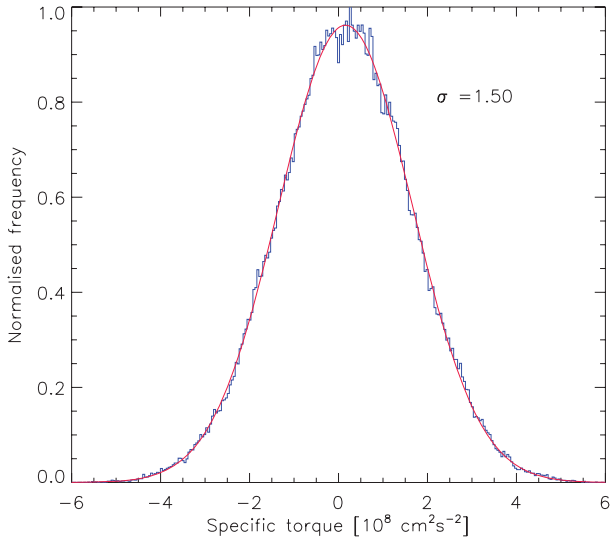

Figure 22. Distribution of torques experienced by the 10 km sized planetesimals in run G1, averaged over all planetesimals. The standard deviation obtained for the distribution $\sigma = 1.5 \times 10^8$ cm^2 s^{-1}.

units). The correlation time, $\tau_{\rm corr}$, was estimated to be $\tau_{\rm corr} = 0.32$ orbits from the exponential decay of the ACF shown in Fig. 9 in Section 3.3.1. The diffusion coefficient, D_j, expressed in code units is given by $D_j = 9.51 \times 10^{-9}$, which leads to the prediction that a typical planetesimal located at $r = 2.5$ (5 au) in model G1 will diffuse such that $\Delta a/a = 0.021$. Comparing this with the value of $\sigma(\Delta a/a)$ in Fig. 21, we see that the simulation resulted in $\sigma(\Delta a/a) \simeq 0.03$ after 1200 orbits, in reasonable agreement with the value predicted by the diffusion coefficient. The fact that the estimated amount of diffusion is too small by a factor of $\sim\sqrt{2}$ compared to the simulation result indicates that the approximation to the diffusion coefficient given by $D_j = \sigma_{\rm T}^2 \tau_{\rm corr}$ is too small by a factor of $\simeq$2. This possibly arises because of the ambiguity discussed in Section 3.3.1 regarding the definition of the correlation time, but may also be affected by sampling errors that arise from using only 25 particles per size bin, leading to Poisson errors at the $\sim$20 per cent level.

We can now examine if the gas drag-induced radial drift of the $R_{\rm p} = 10$ m bodies observed in Fig. 20, and the stochastic migration of all larger planetesimals, is expected. According to equation (22) and Fig. 21, stochastic migration causes a relative change in specific angular momentum $\Delta j/j = 0.015$. Putting this value into equation (20) tells us that planetesimals of size $R_{\rm p} \simeq 25$ metres should radially drift due to gas drag and diffuse by a similar distance. Planetesimals which are smaller than this should show strong inward drift, and larger bodies should have their evolution dominated by diffusion. The relative change in semimajor axes for all planetesimals in run G1 plotted in Fig. 20 shows good agreement with this expectation.

Changes in the mean drag-induced radial drift rate due to the turbulence can only be discerned for planetesimals of size $R_{\rm p} = 10$ m in Fig. 20, where the straight black line plotted in the top-left panel shows the trajectory of a planetesimal embedded in a laminar disc. Up to a time of approximately 300 orbits, the mean drift rates of the planetesimals in the turbulent disc closely match the trajectory in the laminar disc. At later times, however, the trajectories diverge, with the drift rates for the planetesimals in the turbulent disc decreasing by about a factor of 3. This is not due to the effects of stochastic forces, which earlier on in the evolution are seen to cause a dispersion of the trajectories around a mean which matches the laminar case closely. Instead, variations in the effective α stress parameter as a function of radius cause radial structuring of the disc, such that peaks and troughs in the mean surface density arise. The slowing down of the radial drift observed in Fig. 20 arises when the planetesimals enter a region of the disc in which the magnitude of the radial pressure gradient decreases. Thus, we observe that significant changes to the radial drift of planetesimals do not occur due to stochastic forcing, but may arise because of radial structuring of the disc due to spatial variations in turbulent stresses, which persist over the run times of the simulations.

If we adopt a typical disc lifetime of 5 Myr (Haisch et al. 2001), then we can estimate the amount of radial diffusion for large ($R_{\rm p} \geq 1$ km) planetesimals during the planet forming epoch. Adopting a diffusion coefficient, D_j, which gives agreement with the amount of radial diffusion observed for 10 km-sized planetesimals in Fig. 21, equation (21) predicts $\Delta j/j = 0.3$, corresponding to a 50 per cent change in the semimajor axis of a typical planetesimal located initially at 5 au. Considering the relative contributions to radial drift of solid bodies from both gas drag-induced migration and diffusion due to the stochastic gravitational field of the disc, we have plotted the evolution times $\tau_{\rm drag}$ and $\tau_{\rm diff}$ in Fig. 23, assuming a 30 per cent change in the specific angular momentum of a planetesimal, using equations (20) and (21). We can see that for evolution times of 5 Myr, the drag and diffusion time-scales are equal for

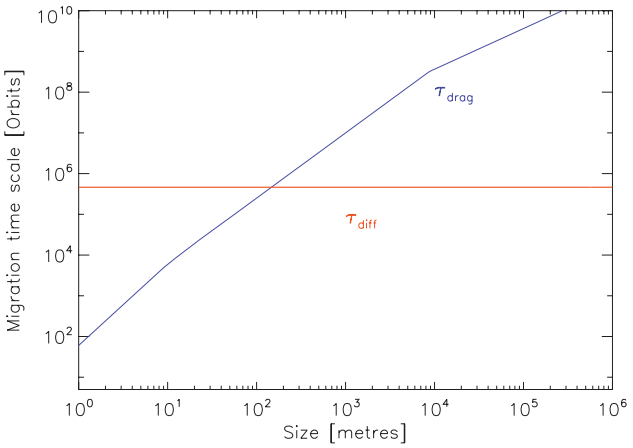

Figure 23. Variation of $\tau_{\rm drag}$ and $\tau_{\rm diff}$ as a function of planetesimal size. The underlying disc model is the same as in run G1.

planetesimal size $R_p \simeq 100$ m, but drag time-scales are much larger than diffusion time-scales for larger bodies such as 1 km and 10 km-sized planetesimals. This shows that large-scale migration of large planetesimals over evolution times of 5 Myr will be dominated by diffusion and not gas drag-induced inward drift.

Strong radial mixing of planetesimals at the level of $\Delta a/a = 0.5$ would have very significant implications for planetary formation. In our own Solar system, for example, radial mixing of large icy planetesimals from beyond the snowline would substantially increase the volatile content of the terrestrial planets, and effectively smear out the observed apparent variation in asteroid properties as a function of heliocentric distance. It thus seems unlikely that such radial mixing occurred in the solar nebula, providing strong circumstantial evidence that the degree of turbulence present in model G1 was not present in the solar nebula during the formation of the Solar system. We explore the degree of radial mixing as a function of turbulent strength (measured by the effective α parameter) below.

3.7.1 Planetesimal diffusion as a function of α

The rms value of the relative change in the semimajor axes for 10 km sized planetesimals for various models is shown in Fig. 21. The discs in models G1 and G5 gave rise to very similar values of α and $\langle \delta\Sigma/\Sigma \rangle$, and we see that the radial diffusion rates are also very similar. Model G3 had a value of $\alpha = 0.017$, and a correspondingly smaller value of $\langle \delta\Sigma/\Sigma \rangle$, which leads to a slower rate of diffusion. The rate of diffusion in semimajor axis is a fairly weak function of α (see discussion below), such that it is only after a time of $t \sim 600$ orbits that the divergence in the diffusion rates can be detected for models G1 and G3 in Fig. 21. Model G4 has a substantially larger value of $\alpha = 0.101$, and leads to a noticeably larger rate of diffusion of $\Delta a/a$ in Fig. 21.

We have fit the data for $\sigma(\Delta a/a)$ shown in Fig. 21 assuming a simple random walk model $\sigma(\Delta a/a) = C_\sigma(\Delta a)\sqrt{t}$, and the coefficients $C_\sigma(\Delta a)$ are given in Table 1. If we fit the data given in Table 1 for α and $C_\sigma(\Delta a)$ using the function $C_\sigma(\Delta a) = K_{\Delta a}\alpha^q$, then the best-fitting solution gives $q = 0.20$ and $K_{\Delta a} = 1.70 \times 10^{-3}$. This is the same power-law dependence found for the evolution of the velocity dispersion as a function of α. This fit allows us to estimate the amount of radial diffusion that we expect as a function of α.

3.7.2 Radial diffusion constraints on α in the solar nebula

As discussed above, large planetesimals experience only small changes in their angular momenta and semimajor axes due to gas drag, assuming that they remain on approximately circular orbits. For example, a 10 km sized planetesimal orbiting at 5 au in model G1, in the absence of turbulence, would migrate a distance of $\sim 4 \times 10^{-3}$ au in 5 Myr. For such large bodies, evolution of the semimajor axis is dominated by turbulence-induced diffusion, especially if the disc is fully turbulent as in models G1–G5. Model G1 predicts that a typical 10 km sized planetesimal orbiting at 5 au will diffuse a distance $\Delta a \simeq 2.5$ au in 5 Myr. If this 50 per cent change in semimajor axis is applied to bodies in the asteroid belt, then this level of diffusion is probably inconsistent with the variation in observed properties of asteroids as a function of heliocentric distance (Gradie & Tedesco 1982; Mothé-Diniz, Carvano & Lazzaro 2003). These variations would have been smeared out substantially if such a large amount of orbital diffusion had taken place during the Solar system formation.

The survey of how the distribution of asteroidal taxonomic types varies as a function of heliocentric distance presented by Gradie & Tedesco (1982) concluded that there is a systematic variation. For the seven taxonomic classes identified in their sample, it was suggested that the distribution of each peaks at a different location in the asteroid belt, with a dispersion around this peak location of 0.5–1 au. The observed correlation between asteroidal type (assumed to relate to composition) and heliocentric distance was interpreted as being evidence that the asteroids were formed essentially in their observed locations, being subject subsequently to a relatively modest amount of radial mixing at the level of $\sim$0.5 au. The more recent survey of Mothé-Diniz et al. (2003) presents a more complicated picture in which S-type asteroids are distributed more uniformly throughout the asteroid belt, but are none the less the dominant class in the inner and middle belts, with the more volatile-rich C-type bodies being preferentially located in the outer belt beyond $\simeq$3 au.

Radial mixing of planetesimals during planet formation is expected to occur through gravitational interaction with planetary embryos. Wetherill (1992) suggested that a population of nearly Mars-mass embryos embedded within the primordial asteroid belt could explain the required mass depletion and radial mixing. More recent simulations of this effect (Petit, Morbidelli & Chambers 2001; O'Brien, Morbidelli & Bottke 2007) show that radial diffusion of asteroids peaks at a value $\Delta a \simeq 0.5$ au, broadly consistent with the observational constraints. In a series of related simulations, O'Brien, Morbidelli & Levison (2006) examined the formation of terrestrial planets, and estimated the rate of water delivery to the Earth by accretion of volatile-rich material from beyond $\sim$2.5 au. It was found that simulations initiated with Jupiter- and Saturn-analogues on circular orbits could reasonably explain the abundance of water on the Earth ($\simeq 5 \times 10^{-4}$ $M_\oplus$). Substantial radial mixing of volatile-rich planetesimals and embryos from the outer asteroid belt, due to disc turbulence, would very likely lead to terrestrial planets which are endowed with water and other volatiles well in excess of what is observed.

We suggest that orbital diffusion due to turbulence which exceeds $\Delta a \simeq 0.5$ au is probably inconsistent with observations, and we now discuss which value of α is consistent with $\Delta a \simeq 0.5$ au in the asteroid belt. It should be noted, however, that using the asteroid belt as a test for dynamical mixing requires that the observed variation of properties with heliocentric distance is primordial. The recent suggestion by Levison et al. (2009) that cometary material originating from further out in the Solar system became implanted in the asteroid belt during the late heavy bombardment means we should take care not to over interpret the observations, or their theoretical implications.

Using the approximate fit $C_{\Delta a} = K_{\Delta a}\alpha^{0.20}$, discussed in Section 3.7.1, combined with $\sigma(\Delta a/a) = C_{\Delta a}\sqrt{t}$, we can estimate which value of α should lead to an amount of diffusion which is consistent with the above discussion. Assuming that the dispersion in asteroid properties as a function of heliocentric distance is consistent with diffusion generating $\sigma(\Delta a/a) = 0.16 (\equiv 0.5/3)$ over a putative solar nebula lifetime of 5 Myr (Haisch et al. 2001), and noting that $K_{\Delta a} = 1.7 \times 10^{-3}$ (see Section 3.7.1), we find an upper limit for $\alpha \simeq 5 \times 10^{-5}$. Interestingly, this is very similar to the midplane Reynolds stress obtained in shearing box simulations of discs with dead zones (Fleming & Stone 2003; Turner, Sano & Dziourkevitch 2007; Ilgner & Nelson 2008). It would seem that our rough estimate for the amount of diffusion which can occur as a function of α provides circumstantial evidence that the solar nebula did indeed contain a substantial dead zone in the vicinity

of the asteroid belt and giant planet formation region. We note, however, that caution must be used when interpreting this result. Confirmation of the variation of diffusion rate as a function of α is required using simulations which include vertical stratification and dead zones, and account needs to be made of the fact that the nebula mass changes significantly over a 5 Myr period. Models for the formation of giant planets require nebula masses approximately three to five times larger than the MMSN (Pollack et al. 1996), which will increase the value of $\sigma(\Delta a/a)$ by a similar factor. The disc mass will deplete over the nebula lifetime, so that the net effect of these competing factors needs to be examined in more detail.

Taken together, the constraints on α lead to some interesting conclusions regarding the strength of turbulence in the solar nebula. Shearing box simulations with dead zones generate Reynolds stresses at the midplane with $\alpha \sim 10^{-5}$. If this stress is accompanied by density waves and stochastic torques with amplitudes which follow the scaling described in Section 3.7.1, then it becomes very difficult to see how runaway growth could have caused rapid growth of planetary embryos *via* planetesimal accretion. Indeed, our results suggest that with $\alpha = 10^{-6}$, catastrophic disruption of 10 km sized bodies remains possible (although this conclusion must await firm confirmation from more realistic, vertically stratified simulations). Taken at face value, this indicates that a mechanism is required for forming large bodies which avoids the need to go through the runaway growth phase, such as that suggested by Johansen et al. (2007). The existence of gradients in the chemical composition of Solar system bodies as a function of heliocentric distance, however, is broadly consistent with a nebula model in which there exists a dead zone with Reynolds stress $\alpha \simeq 10^{-5}$. The existence of these chemical gradients, however, is apparently inconsistent with a fully turbulent disc model with effective $\alpha \gg 10^{-5}$.

3.7.3 Evolution of the eccentricity and $\Delta a/a$

For small values of the eccentricity, the relation between the rms eccentricity, $\sigma(e)$, and the radial velocity dispersion, $\sigma(v_r)$, may be approximated as $\sigma(e) \simeq \sigma(v_r)/v_K$, where v_K is the Keplerian velocity. In Section 3.6.2, we showed that for the larger planetesimals with $R_p = 10$ km, the radial velocity dispersion may be approximated as a random walk with $\sigma(v_r) = C_\sigma(v_r)\sqrt{t}$, where $\sigma(v_r)$ is measured in units of the local sound speed, c_s, and the $C_\sigma(v_r)$ values are listed in Table 1. Similarly, we have shown in Section 3.7.1 that the rms radial diffusion $\sigma(\Delta a/a) = C_\sigma(\Delta a)\sqrt{t}$, where the $C_\sigma(\Delta a)$ values are also listed in Table 1. Thus, we expect the ratio of eccentricity changes to semimajor axis changes, $\sigma(e)/\sigma(\Delta a/a) = (H/r)C_\sigma(v_r)/C_\sigma(\Delta a)$. Taking the value $H/r = 0.05$ for the models G1–G4, we find that $0.34 \leq \sigma(e)/\sigma(\Delta a/a) \leq 0.57$, so that changes in the relative semimajor axes are similar to eccentricity changes for larger planetesimals that are subject to stochastic gravitational interaction with a turbulent disc.

3.7.4 Diffusion versus type I migration of low-mass protoplanets

In addition to considering the radial drift of planetesimals due to gas drag, and the role of stochastic torques in potentially inhibiting this inward drift, we can also consider the effect that these stochastic torques might have on the type I migration of low-mass planets (Nelson & Papaloizou 2004; Nelson 2005). We have ascertained above that bodies undergoing diffusion due to stochastic torques may change their semimajor axes by 50 per cent over a disc lifetime of 5 Myr. Using the type I migration formula from Tanaka, Takeuchi & Ward (2002) for a disc model with properties which are the same as model G1, we note that planets with $m_{pl}/M_\star = 3.5 \times 10^{-7}$ will migrate a distance equal to 50 per cent of their initial semimajor axis (assumed to be 5 au) *via* type I migration over 5 Myr. This indicates that direct competition between type I migration and stochastic migration will only prevent the large-scale migration of planetary bodies with masses similar to that of Mars over such nebula lifetimes. It should be noted, however, that the possible radial structuring of protoplanetary discs by turbulence due to spatial variations in α (possibly due to a dead zone) may provide a means of preventing inward drift due to the operation of corotation torques (Masset 2001; Masset et al. 2006).

3.8 Migration of planetesimals – local model

The local shearing box approximation that we have adopted in this work does not include the effect of a radial pressure gradient in modifying the orbital angular velocity of the gas. Consequently, the gas and embedded bodies orbit at the same mean angular velocity, and planetesimals do not undergo radial migration due to gas drag interaction with a sub-Keplerian disc. Large planetesimals, whose interaction with the gas disc is gravity dominated, experience stochastic gravitational forces that cause diffusion of the semimajor axes (or equivalently, the guiding centres of the particle epicycles). Smaller bodies, whose evolution is dominated by gas drag, similarly diffuse radially due to the stochastic gas drag forces. We discuss both of these regimes below.

3.8.1 Diffusion of gravity dominated bodies

As with the larger planetesimals discussed in Section 3.7 for the global models, the larger planetesimals in the shearing box simulations undergo radial diffusion due to the stochastic gravitational forces they experience. The deviation in the positions of the guiding centres of particles from their initial values is denoted as Δx (measured in units of the local scaleheight H), and we plot the standard deviation of this quantity for the gravity-only particles (set 'G') in Fig. 24. As with the global simulations, the evolution of Δx displays random walk behaviour. As is illustrated by the fitted curve and error bounds in Fig. 24, the random walk can reasonably be

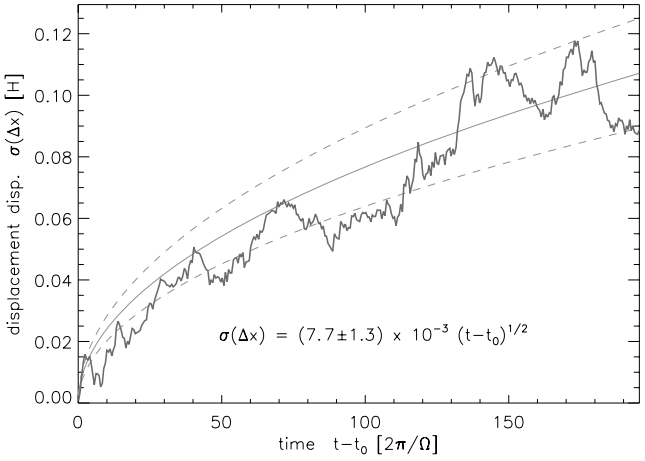

Figure 24. Dispersion in the radial displacement Δx for a swarm of particles subject to the gas gravity alone. The time evolution follows a random walk as reasonably well described by the given relation.

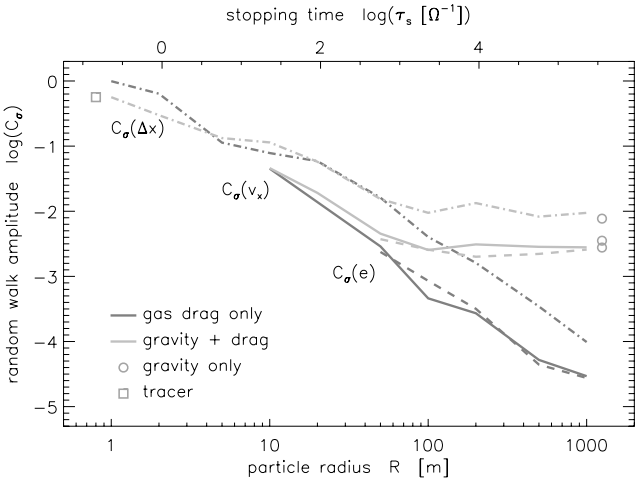

Figure 25. Excitation amplitudes for the random walk behaviour shown in Fig. 24; lines correspond to C_σ for the displacement (dash–dotted), the rms velocity (solid), and the eccentricity (dashed lines). Units are in $[H]$, $[c_s]$ and $[H/R]$ times $[(2\pi/\Omega)^{-1/2}]$, respectively. (These values are also listed in Table 2.)

well approximated by the function

$$\sigma(\Delta x) \approx C_\sigma(\Delta x)\sqrt{t - t_0}, \tag{23}$$

with a single fitting constant $C_\sigma = (7.7 \pm 1.3) \times 10^{-3}$ representing the strength of the stirring mechanism.

The amplitude of this fitting constant for the G+D particle set is plotted using the light grey dash–dotted curve in Fig. 25 (which also displays random-walk fitting parameters for the growth of the radial velocity dispersion and eccentricity). It is clear that for particles with $R_p \geq 100$ m, this coefficient has an almost constant value, indicating that the radial diffusion of these larger-sized planetesimals is dominated by gravitational interaction with the disc. The transition region is rather narrow, and G+D particles quickly approach the values corresponding to the gravity only particle set.

We now compare the results shown in Fig. 24 with those obtained for the global simulations. The deviation of the position of the particle guiding centres is measured in units of the local scaleheight, H. We see from Fig. 24 that the best fit reaches a value $\Delta x = 0.107H$ after a time $t = 200$ orbits, and would reach a value $\Delta x = 0.262H$ after 1200 orbits. Dividing by the initial radial location of the particles, we obtain $\Delta x/r = 0.262H/r$. The shearing box runs have a value $H/r = 0.075$, when we consider that they are located at an orbital radius $r = 5$ au, such that $\Delta x/r = 0.02$. This compares reasonably well with the results of the global simulations, where we obtain a value of $\Delta a/a = 0.03$ for model G1 at $t = 1200$ orbits. In terms of physical parameters, model G5 is the most similar to the shearing box simulation, but as may be seen in Fig. 21, the rate of radial diffusion for models G1 and G5 is very similar.

As discussed in Section 3.7, the diffusion coefficient associated with the random walk in radius of the particles (or equivalently the diffusion of angular momentum) $D_j = \sigma_T^2 \tau_{corr}$, where σ_T is the standard deviation of the fluctuating torque and τ_{corr} is the torque correlation time, averaged over the ensemble. The diffusion coefficient in the global simulations was found to be in reasonable agreement with the degree of particle diffusion obtained in those models. For the shearing box model, the value of σ_T is given in Fig. 7, and is almost identical to that obtained in the global model G1. The torque correlation time is given by Fig. 9, and has a value $\tau_{corr} = 0.32$ orbits. We thus see that the value of $\Delta x/r = 0.02$ obtained by extrapolating Fig. 24 to a time $t = 1200$ orbits is in very good agreement with what would be expected from the diffusion coefficient $D_j = \sigma_T^2 \tau_{corr}$, the prediction being $\Delta x/r = 0.021$.

3.8.2 *Diffusion of gas drag-dominated bodies*

As with the gravity-dominated particles, the gas drag-dominated particles diffuse radially over time. The radial displacement, Δx, evolves according to a random walk, and can be reasonably well fit by equation (23). The fitting coefficients, $C_\sigma(\Delta x)$, are plotted in Fig. 25 as a function of planetesimal size. In Table 2, we furthermore compile a collection of values for reference. We observe that the diffusion via drag forces roughly scales with stopping time like τ_s^{-1} for $\tau_s \ll 1$. When the stopping time approaches the dynamical time Ω^{-1}, which is the case for boulders of a few metres in radius, the dependence on τ_s becomes weaker because the particles are tightly coupled to the turbulent motion of the flow, and essentially behave like massless tracers. In this limit we see that $C_\sigma(\Delta x)$ approaches the value of the tracer particles in Fig. 25.

To interpret the above findings in a more general context and be able to scale the obtained values with respect to model parameters, we now consider the Schmidt number, denoted as $\mathrm{Sc} = \nu/D$.[4] This is the ratio of the momentum diffusion rate and the mass diffusion rate, and in our case the momentum diffusion ν is given by the turbulent Maxwell and Reynolds stresses as quantified by the dimensionless α parameter. For the mass diffusion, we distinguish between Lagrangian fluid elements (represented by massless tracer particles) for which we obtain a diffusion coefficient D_g, and planetesimals with inertia, to which we assign the notation D_p.

Lagrangian tracers. Before looking at the diffusion of the planetesimals themselves, we need to provide a reference value. This is given by $\mathrm{Sc}_g = \nu/D_g$, i.e. the Schmidt number for Lagrangian fluid elements. To determine the diffusion coefficient D_g, we closely follow the approach described in section 4 of Fromang & Papaloizou (2006). This means, we compute the velocity ACF

$$S^{ij}(\tau) = \langle v_i(z(z_0, \tau), \tau)\, v_j(z_0, 0)\rangle\,, \tag{24}$$

where the dependence of v_i on $z(z_0, \tau)$ implies that we are considering the correlation with respect to a Lagrangian fluid element. Note that Fromang & Papaloizou have approximated this by $v_i(z_0, \tau)$, i.e. the Eulerian velocity components (cf. their section 2.3). Because we include the evolution of massless tracer particles, we do not rely on this approximation and can directly compute equation (24) along the particle trajectories.

The diffusion of a fluid element along the radial direction can then be obtained by time-integrating the corresponding component of the correlation tensor:

$$D_g(\tau) = \int_0^\tau S_g^{xx}(\tau')\,\mathrm{d}\tau'\,. \tag{25}$$

As discussed in Fromang & Papaloizou (2006), for large τ this can be approximated by the product of the square of the rms velocity $\langle v_x^2\rangle = S_g^{xx}(0)$ and the correlation time τ_c of the turbulence. This estimate is based on the assumption that the correlations in velocity decay like $\mathrm{e}^{-\tau/\tau_c}$. To check whether this assumption is warranted, we plot $S_g(\tau)$ and the derived $D_g(\tau)$. This is done separately for the x and y directions in the left- and right-hand panels of Fig. 26.

Looking at the two 'hockey stick' shaped curves, we see that the $\mathrm{e}^{-\tau/\tau_c}$ law (dashed lines) is met well for the azimuthal component

[4] To avoid further confusion, we adhere to the conventions introduced in section 2.1 of Youdin & Lithwick (2007).

Table 2. Random walk-amplitudes C_σ describing the stochastic excitation (as depicted in Fig. 24) of the dispersion within an ensemble. Values are obtained for the displacement Δx, the rms radial velocity dispersion, v_x, and the eccentricity e. With the exception of the first column, the applicability of the functional form $C_\sigma (t - t_0)^{1/2}$ is of course limited to the time interval before saturation is reached (see Figs 13 and 14).

	Gravity only	Gravity + drag			Drag force only			Tracer
$[(2\pi/\Omega)^{-1/2}] \times$		10 m	100 m	1 km	10 m	100 m	1 km	
$C_\sigma(\Delta x)$ $[10^{-2} H]$	0.77 ± 0.13	11.4 ± 0.02	0.95 ± 0.11	0.94 ± 0.10	7.71 ± 0.03	0.44 ± 0.12	0.01 ± 0.18	56.5 ± 0.01
$C_\sigma(v_x)$ $[10^{-3} c_s]$	3.53 ± 0.03	45.9 ± 3.75	2.54 ± 0.36	2.79 ± 0.04	45.1 ± 3.10	0.46 ± 0.01	0.03 ± 0.00	—
$C_\sigma(e)$ $[10^{-3} H/R]$	2.77 ± 0.53	—	2.57 ± 0.04	2.58 ± 0.01	—	0.85 ± 0.01	0.03 ± 0.00	—

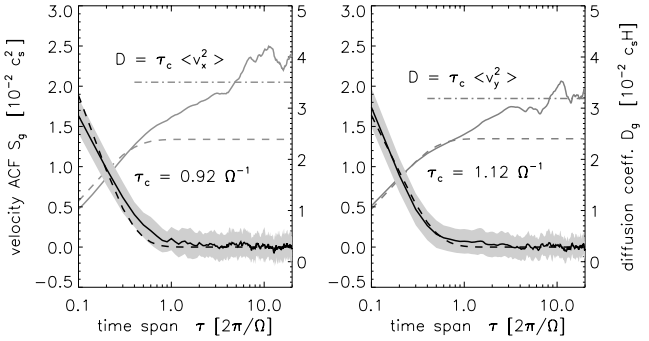

Figure 26. Velocity ACFs S_g^{xx} (left-hand panel) and S_g^{yy} (right-hand panel) for massless tracers. From the ACFs (black lines, LHS axes), we obtain time-integrated diffusion coefficients $D_g(t)$ (grey line, RHS axes). The fits $S_g \sim e^{-\tau/\tau_c}$ (dashed black) result in corresponding diffusion profiles (dashed grey) which agree for $\tau \lesssim 2\pi/\Omega$. For $\tau \gg 1$, D_g can be approximated by the given theoretical estimate (dash–dotted line).

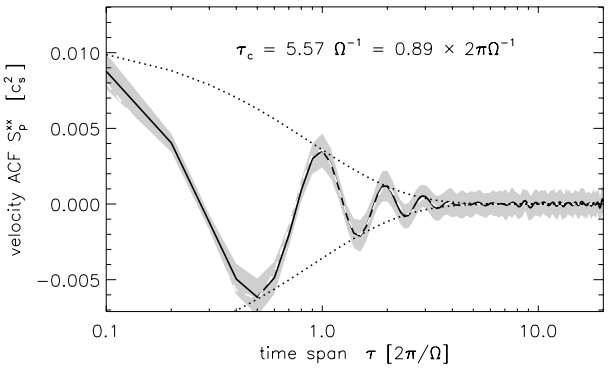

Figure 27. Velocity ACF $S_p(\tau)$ (solid black line) for particles with radius $R = 5$ m. The exponential decay is now modulated by epicyclic oscillations and can be fitted via a function $\sim \cos(2\pi\tau\Omega^{-1})\, e^{-\tau/\tau_c}$ (white dashed line). The envelope (dotted lines) is assumed to be relevant for the diffusion of the guiding centre.

(right-hand panel), whereas there is considerable tension for the radial direction (left-hand panel). Note that the time domain has logarithmic scaling, which implies that the deviation in the shape of the curve cannot be accounted for by changing the fit parameter τ_c. Tentatively, an exponential decay law can be restored via transformation to a generalized time variable $\tilde{\tau} \to \tau^\alpha$ with $\alpha \simeq 0.7$ – we however leave it open whether the observed issue bears any relevance at the current stage of modelling.

Our fitted correlation times are $\tau_c^{(x)} = 0.92\,\Omega^{-1} = 0.15 \times 2\pi\Omega^{-1}$ and $\tau_c^{(y)} = 1.12\,\Omega^{-1} = 0.18 \times 2\pi\Omega^{-1}$. The obtained numbers are in fact very close to the value of 0.15 orbits, reported in Fromang & Papaloizou (2006). This supports the notion that τ_c is characteristic for MRI-typical Mach numbers and only weakly depends on the actual amplitude of the turbulent stresses.

The relation from equation (25) is illustrated by solid grey lines in Fig. 26, which represent the diffusion 'constant' D_g as a function of time. For comparison, we also plot the diffusion profile corresponding to the fitted solution (dashed grey lines). These curves reasonably approximate the τ dependence of D_g for $\tau \lesssim 2\pi/\Omega$. Note, however, that the fitted amplitude is somewhat smaller than the rms velocities and the curves saturate at a lower value. This means that the real correlation functions have a (stochastic) tail that leads to a further growth in D_g for $\tau \gtrsim 2\pi/\Omega$.

For times sufficiently greater than the correlation time of the flow, the diffusion coefficient approaches a constant value approximated by $\tau_c \langle v^2 \rangle \simeq 0.035$ as indicated by dash–dotted lines in the two panels of Fig. 26. In accordance with a recent study by Madarassy & Brandenburg (2010), the observed anisotropy in the streamwise and cross-stream directions is rather weak.

Translated into a Schmidt number, we yield a value of $\mathrm{Sc_g} \simeq 1.6$, which is considerably lower than the ratio between the Maxwell and Reynolds stress, which fluctuates between 3 and 4. Our value is a factor of about 2 smaller than the Eulerian value for *vertical* diffusion found by Fromang & Papaloizou (2006). Schmidt numbers obtained for small particles are usually inferred to be of the order of unity (Johansen & Klahr 2005; Turner et al. 2006), and our results are compatible with this.

A Schmidt number of the order of unity implies that small dust grains that are strongly coupled to the gas will diffuse over large distances during protostellar disc lifetimes. Observations of crystalline silicates embedded in circumstellar discs at significant distances from their host stars, where temperatures are too low to explain in situ crystallization of amorphous grains (van Boekel et al. 2004), suggest that turbulent diffusion may indeed be responsible for transporting grains from the hot inner regions of discs to the cooler outer regions. It remains to be demonstrated, however, in a global, turbulent disc model, whether or not a substantial number of grains can be transported outwards against the net inward mass accretion flow on to the star.

Particles with inertia. Unlike massless tracers, real particles are subject to the additional body forces in the rotating coordinate frame. Consequently, this leads to the excitation of epicyclic oscillations. In the case of the Keplerian rotation, the associated angular frequency κ is identical with the local rotation rate Ω. The ACF for a perfect epicyclic oscillation is then simply proportional to $\cos(2\pi\tau\Omega^{-1})$. This means that velocities are maximally correlated if they are apart by a full period, and anti-correlated in between.

In general, the particles' motion will, however, deviate from a perfect epicycle – or, in other words, the defining elements of the motion will change stochastically. With both the eccentricity and the position of the guiding centre fluctuating, the coherence of the motion is lost for larger times. This is illustrated in Fig. 27, where we plot the velocity ACF for particles of size $R_p = 5$ m. The epicyclic nature of the particle motion is clearly seen in the

Table 3. Time-scales and Schmidt numbers $\mathrm{Sc_p} = \alpha_{ss}\, c_s H/D_p$ for the diffusion of the guiding centres of heavy particles on excited epicyclic orbits.

$R_p =$	1 m	2 m	5 m	10 m	20 m
$\tau_s\,(\Omega^{-1})$	0.23	0.91	5.71	22.8	91.4
$\tau_c\,(\Omega^{-1})$	0.68	1.59	5.74	16.7	46.4
τ_s/τ_c	2.96	1.74	1.01	0.73	0.51
$\mathrm{Sc_p}$	4.22	27.5	45.3	96.4	182.

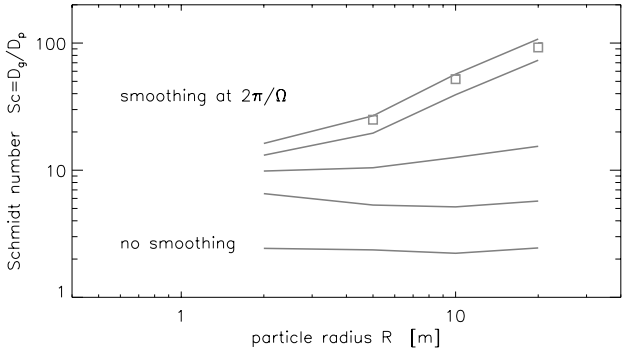

Figure 28. Attempt to determine the Schmidt number $\mathrm{Sc} = D_g/D_p$ for the diffusion of the guiding centres. The diffusion coefficient is estimated via $D_p \simeq \tau_c \langle v_{gc}^2 \rangle$, where v_{gc} is obtained by smoothing over the epicycles (solid lines). An alternative estimate (open squares) is derived independently via the coefficients $C_\sigma^2(\Delta x)$ in Table 2 – note that these do not depend on any form of smoothing.

sinusoidal modulation of S_p. If integrated over time, the 'diffusion' process would rather resemble a shaking motion than a random walk.

As a result, this renders the direct integration approach illustrated in Fig. 26 difficult. Taking the excellent agreement with the functional dependence $\sim \cos(2\pi\tau\Omega^{-1})\,\mathrm{e}^{-\tau/\tau_c}$, we however conjecture that the diffusive part of the overall motion can be recovered from the exponential envelope function (dotted line in Fig. 27). In Table 3, we report this correlation time as a function of particle radius R_p and compare[5] it to the stopping time τ_s. The ratio τ_c/τ_s is about unity for $R_p = 5$ m and roughly scales with the square-root of the radius.

Given we can obtain a good estimate for the rms velocity of the guiding centres, we can then compute $D_p \simeq \tau_c \langle v_{gc}^2 \rangle$. Looking at Fig. 11, it seems less than straightforward to deconvolve the random motion of the guiding centre from the overall motion, especially since the amplitude of the epicycles changes on comparable time-scales. As a first attempt, we simply smooth out the oscillations applying a box-car filter in time. The thus derived Schmidt number $\mathrm{Sc} = D_g/D_p$ as a function of particle size is plotted in Fig. 28 for various values of the filter size.

If we omit the smoothing, the results (although not strictly correct) reflect the kinetic energy in the epicyclic mode itself. In this case, the gradual decoupling of the particles implies that $\langle v^2 \rangle$ decreases while τ_c increases accordingly. Interestingly, this leaves the overall particle diffusion rate unchanged. If we increase the filter size, the epicyclic motion is attenuated and the size dependence gradually becomes steeper. Reasonable convergence is obtained when the filter size approaches the critical value, equal to the epicyclic period. In Table 3, we list the corresponding numbers.

Note that already for metre-sized objects the particle diffusivity is reduced relative to Lagrangian tracers. We attribute this to the effect that part of the kinetic energy is absorbed in ordered epicyclic motion and is thus not available for particle diffusion (cf. section 3.2 in Youdin & Lithwick 2007). The partial slippage of the particles through the gas as a result of weaker drag acceleration also causes the particle guiding centre velocities to be reduced relative to the fluid turbulent velocities.

It might be seen as a deficiency of the approach that it depends on the proper choice of a box-car filter function. To reinforce the validity of the derived Schmidt numbers, we therefore provide an independent estimate from the squares of the coefficients $C_\sigma(\Delta x)$ from Fig. 25. Defining the growing spread in the particles position with time, these can similarly be interpreted as a diffusion constant. For consistency, we have also checked that the fit constants $C_\sigma(\Delta x)$ do not change significantly, when the epicyclic part of the motion is smoothed. Considering that this second estimate solely relies on positions while the original one is derived from velocity correlations, the agreement seen in Fig. 28 (where we plot the different estimates for the Schmidt number) is quite striking.

4 CONCLUSIONS

We have presented results from both local and global MHD simulations which examine the evolution of planetesimals and boulders of different size embedded in turbulent protoplanetary disc models. The main aims of this work are to: determine the magnitude of the velocity dispersion which is excited in a planetesimal swarm; determine the rate of radial diffusion of the planetesimals; determine under which conditions broad agreement is obtained in the results from local shearing box simulations and global disc simulations.

We find that the magnitude of density fluctuations, and the associated stochastic forces experienced by embedded planetesimals, is sensitive to the dimensions of shearing box models. This appears to be related to the fact that accurate modelling of the excitation and non-linear steepening of spiral density waves requires boxes which are elongated in the azimuthal direction (Heinemann & Papaloizou 2009b). The two-point correlation function for the perturbed surface density also shows that coherent structures stretched by a distance $\simeq 6H$ are a common feature of MHD turbulence in discs, indicating that shearing boxes in excess of this length-scale are required to prevent the premature truncation of the gravitational field which results from these structures. In addition to the magnitude of the stochastic torques being dependent on the box size, we also found that the correlation time of the fluctuating torques also depends on the box size and aspect ratio, with smaller boxes generating shorter correlation times. This is apparently due to the ability of waves to propagate across the box on multiple occasions due to the periodic boundary conditions employed, combined with the rate at which they shear past the planet due to the background flow. Shearing boxes with dimensions $4H \times 16H \times 2H$ were found to provide converged results which agree well with the results from global simulations.

We find that both global simulations and local shearing box simulations predict that rapid excitation of planetesimal random velocities is expected in fully turbulent disc models whose local surface densities are similar to the MMSN. A model whose turbulent stresses generate $\alpha = 0.035$ leads to rapid growth of the radial velocity dispersion, $\sigma(v_r)$, *via* a random walk, such that after 1200 orbits at 5 au $\sigma(v_r) = 200\,\mathrm{m\,s^{-1}}$. A model with weaker turbulence

[5] The ratio τ_s/τ_c should not be confused with the Stokes number $\mathrm{St} = \tau_s/\tau_e$ which measures the particle coupling with respect to the eddy velocity.

($\alpha = 0.017$) gave rise to $\sigma(v_r) = 166\,\mathrm{m\,s^{-1}}$ over the same evolution time. These random velocities are much larger than either the escape velocities from planetesimals with sizes 1 or 10 km or the catastrophic disruption thresholds for collisions between bodies of similar size (Benz & Asphaug 1999; Stewart & Leinhardt 2009), suggesting that planetesimal collisions occurring in fully turbulent discs similar to those considered in this paper will result in the destruction of the planetesimals. We find that the expected equilibrium velocity dispersion for 10 km sized planetesimals scales weakly with the turbulent stress parameter such that $\sigma(v_r) = K_{v_r}\alpha^{0.2}$. Extrapolation of the simulation results presented in this paper to low values of α suggests that even with $\alpha = 10^{-6}$, bodies with size 10 km are likely to have random velocities which will cause catastrophic disruption during mutual collisions. Values of $\sigma(v_r)$ small enough to allow runaway growth of planetesimals to occur will be even more difficult to achieve. For smaller bodies, which are more tightly coupled to the gas *via* gas drag, we find that the equilibrium velocity dispersion decreases, and reaches a minimum of $\sigma(v_r) \simeq 20\,\mathrm{m\,s^{-1}}$ for bodies of size 50 m in a disc with $\alpha = 0.035$. For smaller bodies than these the increasing influence of gas drag causes the velocity dispersion to increase with decreasing size, and boulders with $R_p = 1$ m develop random velocities which closely match the turbulent gas motions.

In addition to driving the growth of the velocity dispersion, or equivalently the eccentricity, the stochastic forces experienced by the planetesimals cause them to diffuse radially through the disc. For large planetesimals with $R_p = 10$ km, radial drift through the disc due to gas drag occurs very slowly, and their radial motion is expected to be dominated by diffusion caused by the stochastic gravitational field of the turbulent disc. Indeed, after a putative disc lifetime of 5 Myr, the rms relative change in semimajor axis, $\sigma(\Delta a/a)$, for a planetesimal swarm located at 5 au in a disc with $\alpha = 0.035$ will be 50 per cent, which would have been sufficient to cause large-scale migration of the small body populations of the Solar system during its formation. The fact that such large-scale migration of large planetesimals does not appear to have happened allows us to put constraints on the strength of α in the solar nebula. A value of $\alpha \simeq 10^{-5}$ would lead to a more reasonable $\sigma(\Delta a/a) \simeq 0.1$, consistent with the notion that the solar nebula had a dead zone in the region where planet formation took place.

Smaller planetesimals with $R_p = 10$–100 m are expected to undergo large-scale radial drift due to gas drag, and this is observed in our simulations. The migration rate of 10 m size bodies in the turbulent discs, relative to that expected for an equivalent laminar disc model, is found to be very similar. Migration in turbulent discs is found to be slower by a factor of approximately 2–3, and this is due to radial structuring of the disc's density profile, creating regions where the pressure gradient (and hence rotational velocity profile) is modified.

There have been a number of previous studies of the dynamical evolution of planetary bodies embedded in turbulent discs. Nelson & Papaloizou (2004) examined the torques experienced by low-mass planets and suggested that random walk behaviour for such bodies should be expected, as has been observed in this paper. Nelson (2005) examined the orbital evolution of planets embedded in turbulent discs, with particular emphasis on the semimajor axis and eccentricity changes. The strength of the turbulence in that model was somewhat weaker than considered in this paper ($\alpha \simeq 5 \times 10^{-3}$), although the disc model was somewhat more massive, and in general it was found that the response of embedded bodies to the stochastic forcing was stronger in that study, with larger changes in semimajor axis and eccentricity being observed. The primary reason for this discrepancy appears to be the fact that a persistent vortex formed in the disc model considered by Nelson (2005). Such vortices were also reported in the work of Fromang & Nelson (2005), and interaction between embedded bodies and such structures can lead to significant modification of the semimajor axes and excitation of eccentricity. The models presented in this paper do not have such vortex features, but during the early stages of this project disc models with lower values of α were found to generate such flow features quite readily. One possibility is that global disc models which are close to the limits of resolving the MRI generate substantial variations in α as a function of radius, which in turn generate localized pressure maxima which are particularly prone to the formation of vortices (Hawley 1987; Lovelace et al. 1999). Models with smaller values of the plasma β parameter have stronger field strengths and thus resolve the MRI more easily, and in addition the stronger fields may act to inhibit vortex formation through the action of local magnetic stresses. We have considered these models in this paper.

Yang et al. (2009) recently considered the evolution of planetesimal swarms using non-stratified shearing box simulations. The planetesimals in that study experienced the fluctuating gravitational field of the disc, but did not experience gas drag forces. Although random walk behaviour of the particles in that study was observed, in general it was found to be significantly weaker than we report here, and one conclusion reached by these authors is that turbulence is unlikely to cause the catastrophic disruption of planetesimals. The primary reason for this appears to be the fact that most simulations performed by Yang et al. (2009) used shearing boxes with $2H \times 2H \times 2H$. Test calculations with larger boxes presented in that paper indicated a strong increase in the response of the particles to the turbulence forcing as a function of increasing box size, suggesting that the main reason for the discrepancy between the results is due to this effect.

Ida et al. (2008) recently considered the evolution of planetesimals embedded in turbulent protoplanetary discs by means of N-body simulations combined with a prescription for planetesimal stirring based on the work of Laughlin et al. (2004). In basic agreement with the results we have presented in this paper, they show that turbulence leads to the excitation of a large velocity dispersion, which is likely to cause catastrophic disruption of planetesimals rather than growth following mutual collisions, for a wide range of turbulent strengths.

The simulations we have presented here use the simplest possible numerical set-up: ideal MHD in non-stratified disc models. In a future paper we will present the results of a similar study using vertically stratified models with and without dead zones. This future study will tell us whether we need to examine new paradigms for the rapid growth of planetesimals, or whether instead runaway growth can indeed occur within a dead zone of an otherwise turbulent protoplanetary disc.

ACKNOWLEDGMENTS

OG thanks Sebastien Fromang for discussions on improving the numerical scheme and providing his spectral analysis tools. RPN thanks Alessandro Morbidelli and Bill Bottke for discussions about the radial mixing of asteroids. This work used the NIRVANA-III code developed by Udo Ziegler at the Astrophysical Institute Potsdam. All computations were performed on the QMUL HPC facility, purchased under the SRIF initiative. RPN and OG acknowledge the hospitality of the Isaac Newton Institute for Mathematical Sciences, where most of the work presented in this paper was completed during the 'Dynamics of Discs and Planets' research programme.

REFERENCES

Adams F. C., Bloch A. M., 2009, ApJ, 701, 1381
Adams F. C., Laughlin G., Bloch A. M., 2008, ApJ, 683, 1117
Armitage P. J., 1998, ApJ, 501, L189
Bai X., Stone J. M., 2010, preprint (astro-ph/1005.4982)
Balbus S. A., Hawley J. F., 1991, ApJ, 376, 214
Balbus S. A., Hawley J. F., 2006, ApJ, 652, 1020
Balsara D. S., Meyer C., 2010, preprint (astro-ph/1003.0018)
Balsara D. S., Spicer D. S., 1999, J. Comput. Phys., 149, 270
Balsara D. S., Tilley D. A., Rettig T., Brittain S. D., 2009, MNRAS, 397, 24
Baruteau C., Lin D. N. C., 2010, ApJ, 709, 759
Benz W., Asphaug E., 1999, Icarus, 142, 5
Bodo G., Mignone A., Cattaneo F., Rossi P., Ferrari A., 2008, A&A, 487, 1
Davis S. W., Stone J. M., Pessah M. E., 2010, ApJ, 713, 52
de Val-Borro M. et al., 2006, MNRAS, 370, 529
Fleming T., Stone J. M., 2003, ApJ, 585, 908
Flock M., Dzyurkevich N., Klahr H., Mignone A., 2010, A&A, 516, 26
Fromang S., Nelson R. P., 2005, MNRAS, 364, L81
Fromang S., Papaloizou J., 2006, A&A, 452, 751
Fromang S., Papaloizou J., 2007, A&A, 476, 1113
Fromang S., Papaloizou J., Lesur G., Heinemann T., 2007, A&A, 476, 1123
Gammie C. F., 2001, ApJ, 553, 174
Gardiner T. A., Stone J. M., 2005, J. Comput. Phys., 205, 509
Gardiner T. A., Stone J. M., 2008, J. Comput. Phys., 227, 4123
Goldreich P., Ward W. R., 1973, ApJ, 183, 1051
Gradie J., Tedesco E., 1982, Sci, 216, 1405
Gressel O., Ziegler U., 2007, Comput. Phys. Communications, 176, 652
Haisch K. E. Jr, Lada E. A., Lada C. J., 2001, ApJ, 553, L153
Hawley J. F., 1987, MNRAS, 225, 677
Hawley J. F., 2001, ApJ, 554, 534
Hawley J. F., Stone J. M., 1995, Comput. Phys. Communications, 89, 127
Hawley J. F., Gammie C. F., Balbus S. A., 1995, ApJ, 440, 742
Hayashi C., 1981, Progress Th. Phys. Suppl., 70, 35
Heinemann T., Papaloizou J. C. B., 2009a, MNRAS, 397, 52
Heinemann T., Papaloizou J. C. B., 2009b, MNRAS, 397, 64
Ida S., Makino J., 1993, Icarus, 106, 210
Ida S., Guillot T., Morbidelli A., 2008, ApJ, 686, 1292
Ilgner M., Nelson R. P., 2008, A&A, 483, 815
Johansen A., Klahr H., 2005, ApJ, 634, 1353
Johansen A., Oishi J. S., Low M., Klahr H., Henning T., Youdin A., 2007, Nat, 448, 1022
Johansen A., Youdin A., Klahr H., 2009, ApJ, 697, 1269
Johnson E. T., Goodman J., Menou K., 2006, ApJ, 647, 1413
Johnson B. M., Guan X., Gammie C. F., 2008, ApJS, 177, 373
Kokubo E., Ida S., 1998, Icarus, 131, 171
Laughlin G., Steinacker A., Adams F. C., 2004, ApJ, 608, 489
Lesur G., Longaretti P.-Y., 2007, MNRAS, 378, 1471
Levison H. F., Bottke W. F., Gounelle M., Morbidelli A., Nesvorný D., Tsiganis K., 2009, Nat, 460, 364
Lovelace R. V. E., Li H., Colgate S. A., Nelson A. F., 1999, ApJ, 513, 805
Madarassy E. J. M., Brandenburg A., 2010, Phys. Rev. E, 82, 016304
Masset F., 2000, A&AS, 141, 165
Masset F. S., 2001, ApJ, 558, 453
Masset F. S., 2002, A&A, 387, 605
Masset F. S., Morbidelli A., Crida A., Ferreira J., 2006, ApJ, 642, 478
Miniati F., 2010, J. Comput. Phys., 229, 3916
Miyoshi T., Kusano K., 2005, J. Comput. Phys., 208, 315
Mothé-Diniz T., Carvano J. M. Á., Lazzaro D., 2003, Icarus, 162, 10
Nelson R. P., 2005, A&A, 443, 1067
Nelson R. P., Papaloizou J. C. B., 2003, MNRAS, 339, 993
Nelson R. P., Papaloizou J. C. B., 2004, MNRAS, 350, 849
O'Brien D. P., Morbidelli A., Levison H. F., 2006, Icarus, 184, 39
O'Brien D. P., Morbidelli A., Bottke W. F., 2007, Icarus, 191, 434
Ogihara M., Ida S., Morbidelli A., 2007, Icarus, 188, 522
Oishi J. S., Mac Low M., Menou K., 2007, ApJ, 670, 805
Papaloizou J. C. B., Nelson R. P., 2003, MNRAS, 339, 983
Papaloizou J. C. B., Nelson R. P., Snellgrove M. D., 2004, MNRAS, 350, 829
Petit J., Morbidelli A., Chambers J., 2001, Icarus, 153, 338
Pollack J. B., Hubickyj O., Bodenheimer P., Lissauer J. J., Podolak M., Greenzweig Y., 1996, Icarus, 124, 62
Press W. H., Teukolsky S. A., Vettering W. T., Flannery B. P., 1996, Numerical Recipes in Fortran 90: The Art of Scientific Computing. Cambridge University Press, Cambridge
Rafikov R. R., 2004, AJ, 128, 1348
Regev O., Umurhan O. M., 2008, A&A, 481, 21
Rein H., Papaloizou J. C. B., 2009, A&A, 497, 595
Shakura N. I., Syunyaev R. A., 1973, A&A, 24, 337
Sicilia-Aguilar A., Hartmann L. W., Briceño C., Muzerolle J., Calvet N., 2004, AJ, 128, 805
Stewart S. T., Leinhardt Z. M., 2009, ApJ, 691, L133
Stone J. M., Gardiner T. A., 2010, ApJS, 189, 142
Stone J. M., Norman M. L., 1992, ApJS, 80, 753
Tanaka H., Takeuchi T., Ward W. R., 2002, ApJ, 565, 1257
Turner N. J., Sano T., 2008, ApJ, 679, L131
Turner N. J., Willacy K., Bryden G., Yorke H. W., 2006, ApJ, 639, 1218
Turner N. J., Sano T., Dziourkevitch N., 2007, ApJ, 659, 729
van Boekel R. et al., 2004, Nat, 432, 479
van Leer B., 1977, J. Comput. Phys., 23, 276
Ward W. R., 1997, Icarus, 126, 261
Weidenschilling S. J., 1977, MNRAS, 180, 57
Wetherill G. W., 1992, Icarus, 100, 307
Wetherill G. W., Stewart G. R., 1993, Icarus, 106, 190
Winters W. F., Balbus S. A., Hawley J. F., 2003, ApJ, 589, 543
Yang C., Mac Low M., Menou K., 2009, ApJ, 707, 1233
Youdin A., Johansen A., 2007, ApJ, 662, 613
Youdin A. N., Goodman J., 2005, ApJ, 620, 459
Youdin A. N., Lithwick Y., 2007, Icarus, 192, 588
Ziegler U., 2004, J. Comput. Phys., 196, 393
Ziegler U., 2008, Comput. Phys. Communications, 179, 227
Ziegler U., Yorke H. W., 1997, CoPhC, 101, 54

This paper has been typeset from a TEX/LATEX file prepared by the author.